Distribution
Category UC-70

SAND85-7114
LBL-21022

Unlimited Release
Printed October 1986

Hydrologic Mechanisms Governing Partially Saturated Fluid Flow in Fractured Welded Units and Porous Nonwelded Units at Yucca Mountain

J. S. Y. Wang and T. N. Narasimhan

Earth Sciences Division
Lawrence Berkeley Laboratory
University of California
Berkeley, CA 94720

for

Sandia National Laboratories
P.O. Box 5800
Albuquerque, NM 87185

Under Sandia Contract: 64-5958

Sandia Contract Monitor

Y. T. Lin

Geoscience Analysis Division

Abstract

A discrete fracture, porous matrix model and a composite medium model were used to study hydrological responses to cycles of pulse infiltration at Yucca Mountain, a potential site for a nuclear waste repository. The pulses were applied to fractures at the top of a vertical column composed of alternating layers of welded and nonwelded volcanic tuff. For average infiltration rates of 0.1 to 0.5 mm/yr, pulses expressed as short durations separated by periods up to 5,000 yr, the transition from partially saturated conditions to fully saturated conditions and the corresponding onset of fracture flows occur in the top Tiva Canyon welded unit. As water moves down into the Paintbrush nonwelded unit, most effects of the transient infiltration pulse are damped during the first few thousand years. The responses of the underlying Topopah Spring welded unit to the pulses exhibit only small changes in saturation, pressure, and potential from the steady-state values. In addition to the downward motion, some of the infiltrating water may move laterally. Lateral flows in the column model are caused by an assumed fixed gradient in the horizontal direction, corresponding to the eastward dip of the bedding planes. For 0.1 mm/yr average infiltration cases which the fixed-gradient approximation is applicable under steady-state conditions, the infiltration pulses prefer to move essentially downward with a small fraction of water moving laterally.

Acknowledgments

We thank Y. T. Lin and S. Sinnock for discussing the simulations, R. Eaton, R. Peters, G. Bodvarsson, K. Pruess, and Y. Tsang for reviewing the manuscript. This work was supported by the Sandia National Laboratories for the Neveda Nuclear Waste Storage Investigations Project of the U. S. Department of Energy.

Table of Contents

List of Tables

List of Figures

Nomenclature

a_v	compressibility	$[M^{-1}Lt^2]$
$\overline{b}$	effective aperture	$[L^2]$
b_c	contact cutoff aperture	$[L^2]$
D	fracture spacing	[L]
h	pressure head	[L]
k(S)	permeability at saturation S	$[L^2]$
k_s	saturated permeability	$[L^2]$
m	parameter in van Genuchten's formula, $m = 1 - 1/n$	
n	parameter in van Genuchten's formula	
S	saturation	
t	time	[t]
α	parameter in van Genuchten's formula	$[L^{-1}]$
ϕ	porosity	
ω	fraction of surface contact area	

van Genuchten's formula:

$$S = S_r + (1-S_r)\left[\frac{1}{1+(-\alpha h)^n}\right]^m$$

$$\frac{k(S)}{k_s} = \frac{\left\{1-(-\alpha h)^{n-1}\left[1+(-\alpha h)^n\right]^{-m}\right\}^2}{\left[1+(-\alpha h)^n\right]^{\frac{m}{2}}}$$

1.0 Introduction

The work described in this report was performed for Sandia National Laboratories (SNL) as a part of the Nevada Nuclear Waste Storage Investigations (NNWSI) Project. The NNWSI Project is administered by the Nevada Operations Office of the Department of Energy (NVO). The project is part of the DOE's program to safely dispose of the commercial high-level nuclear wastes. The NNWSI Project is evaluating the suitability of Yucca Mountain, on and adjacent to the Nevada Test Site (NTS) in southern Nevada, to determine the feasibility of developing a mined repository for high-level nuclear wastes.

The objective of this work is aiding performance assessment activities at SNL by addressing the hydrologic mechanisms governing fluid flow in partially saturated, fractured, porous tuff at Yucca Mountain. In the first phase of this work, described in Water Resources Research paper (Wang and Narasimhan, 1985), we developed a conceptual model and constructed a general statistical approach for flow of water along fractures and between matrix blocks and adjointing fractures under partially saturated conditions. We used the model to study the drainage of a fractured tuff column, explicitly take into account the discrete fractures and the porous matrix blocks. The results of the previous work indicate that steady-state fluid flow within Topopah Spring Member, the candidate host rock for the repository, occurs mainly through the partially saturated rock matrix. Modeling simulations indicated that transient changes from fully saturated to partially saturated conditions depended strongly on the hydrological properties of the fractures.

In this report, we present results of simulations for the infiltration of water through alternating layers of welded and nonwelded units at Yucca Mountain under steady and transient conditions. Specifically, we (1) present the steady-state solutions of saturation, pressure, potential, conductivity, and Darcy velocity

profiles through the unsaturated zone, (2) study the hydrologic responses of these conditions to pulses of water moving downward across the interfaces between welded and nonwelded units, (3) estimate the magnitude of lateral flow in the nonwelded units, and (4) discuss the approaches of using single continuum and multiple interacting continua to model steady and transient flow in a partially saturated, fractured, porous medium.

2.0 Hydrologic Models

Yucca Mountain consists of alternating units of welded and nonwelded tuff. Based on geologic considerations, the partially saturated zone over most of Yucca Mountain can be divided from top downward into five distinct units: the Tiva Canyon welded unit (TCw), the Paintbrush nonwelded unit (PTn), the Topopah Spring welded unit (TSw), the Calico Hills nonwelded, vitric unit (CHn-v), and the Calico Hills nonwelded, zeolitic unit (CHn-z) (Ortiz et al., 1985; Sinnock, Lin, and Brannen, 1984; Montazer and Wilson, 1984; Rulon, Bodvarsson, and Montazer, 1985; Klavetter and Peters, 1985). Laboratory measurements of the hydrologic properties of matrix blocks and single fractures from core samples are available for all units (Peters et al., 1984). Fracture distributions in borehole cores and surface outcrops have been mapped (Spengler and Chornack, 1984; Scott et al., 1982). The hydrologic properties of large rock volumes in the unsaturated zone are very limited and are estimated from pumping tests in the saturated zone in the vicinity of Yucca Mountain (Thordarson, 1983; Winograd and Thordarson, 1975; Rush et al., 1985; Barr, 1985). Some recent air-permeability tests in the unsaturated zone are discussed in Montazer and Wilson (1984). In the present report, we use data mainly from borehole USW G-4, one of the few holes within the proposed waste emplacement area at Yucca Mountain.

Table 1 summarizes the matrix properties for the five unsaturated tuff units considered in this report. The saturated conductivities and matrix porosities are average values from laboratory measurements of matrix samples (Sinnock, Lin, and Brannen, 1984). The characteristic curves (van Genuchten parameters) correspond to representative samples analyzed by Peters et al. (1984). Table 2 summarizes the fracture parameters used in this report. The fracture spacings are derived from fracture densities and orientations reported for borehole USW G-4 by Spengler and Chornack (1984) (Fig. 1). Fracture-aperture parameters and fracture permeabilities are derived by the procedure described in Wang and Narasimhan (1985) from estimated bulk rock saturated permeabilities given by Thordarson (1983) and Sinnock, Lin, and Brannen (1984) and fracture density and orientation data. The same procedure also determines the fracture-contact cutoff apertures from the fractions of fracture plane where adjoining matrix blocks are in contact. We assumed that the contact areas were identical to the areas where mineral coatings occured in the fractured cores from borehole USW G-4 (Spengler and Chornack, 1984). The fraction of fracture coatings, predominately clay, calcite, and zeolite, increases with depth. This is consistent with the closure of fractures with depth as a result of overburden stress. The USW G-4 fracture data do not distinguish between the vitric and zeolitic Calico Hills units. We assume that the fracture surfaces in the vitric units do not have zeolite coatings and the 15% value (Table 2) corresponds solely to the area of clay and calcite coatings. For the zeolitic unit, an additional 35% of the surfaces are coated with zeolite, making the assumed fracture contact area 50% of the fracture plane. Tables 1 and 2 include compressibility values derived from laboratory stress-displacement measurements of fractured and intact rock samples (Peters et al., 1984; Nimick et al., 1984).

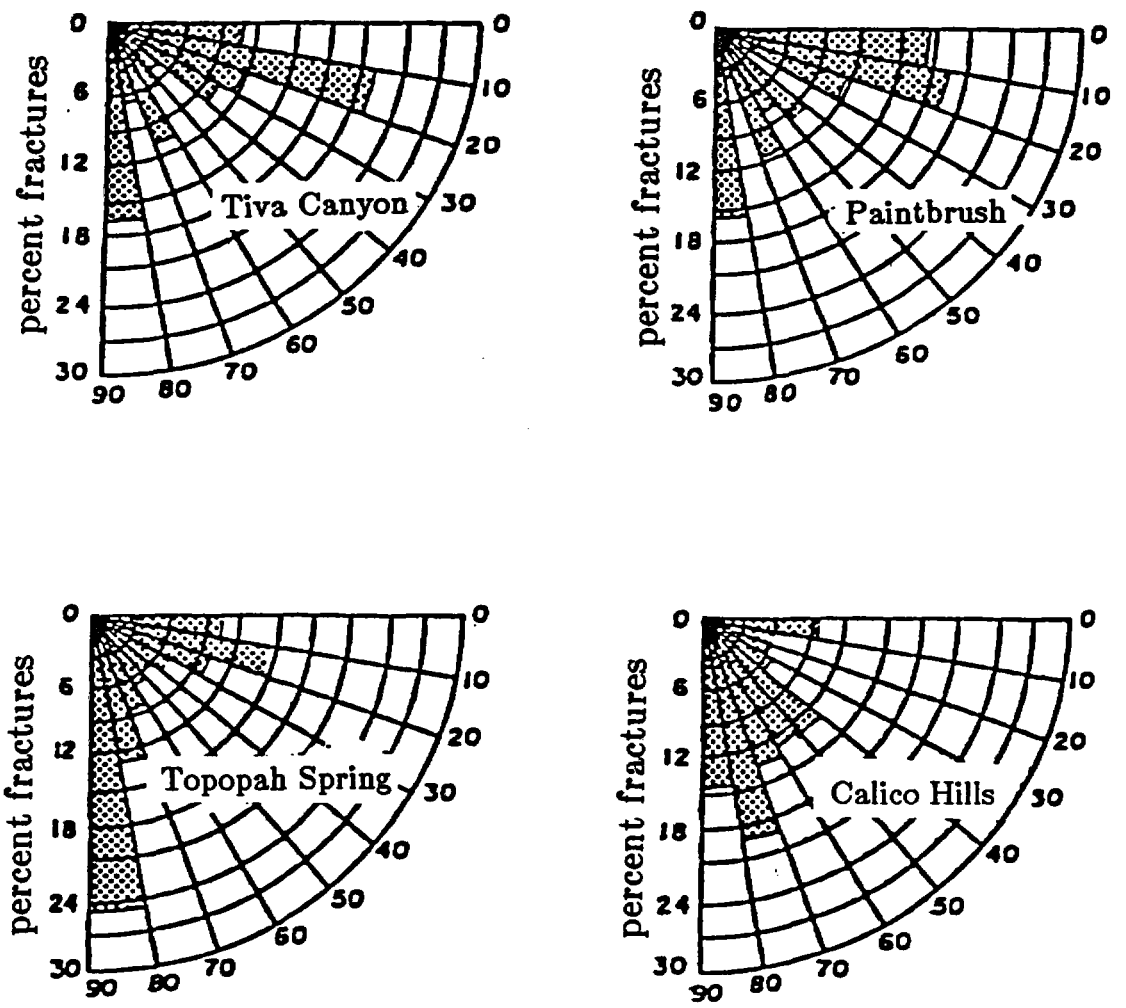

Figure 1. Fracture Inclination of Yucca Mountain Based on Borehole USW G-4 Cores (from Spengler and Chornack, 1984).

Figure 2 depicts the characteristic curves (saturation-pressure relationships) for the matrix (Peters et al., 1984) and the vertical fractures in the five units. As apparent from Figure 2, the fractures in all units easily desaturate with a small suction of -0.1 m to -1. m of pressure head. For the matrix, significant desaturation occurs only when the pressure-heads are in the order of -100 m. For the welded Tiva Canyon unit (Fig. 2a), the welded Topopah Spring unit (Fig. 2c) and the zeolitic Calico Hills unit (Fig. 2e), significant saturations (0.3 or more) can be maintained even with pressure heads in the -1,000 m range. For the nonwelded Paintbrush unit (Fig. 2b) and the vitric Calico Hills unit (Fig. 2d), most of the saturation change occurs over a relatively narrow pressure range around -100 m, indicating a nearly uniform pore-size distribution. Some of the differences in characteristic curves between the welded and nonwelded tuff may be related to deposition processes whereby well-sorted ash falls form the nonwelded units and the microscopically heterogeneous induration processes convert large ash flows into welded tuff (Sinnock, personal communication, 1985).

Table 1. Matrix Properties

Unit	Saturated Permeability k_s (Conductivity [1]) m^2 (mm/yr)	Porosity[1] ϕ	van Genuchten Parameters [2]			Compressibility [3]
			α (1/m)	n	S_r	a_v (1/Pa)
Tiva Canyon Welded	2.55×10^{-18} (0.8)	0.1	8.21×10^{-6}	1.558	0.002	6.32×10^{-11}
Paintbrush Nonwelded	2.45×10^{-15} (760)	0.45	1.50×10^{-2}	6.872	0.1001	8.36×10^{-10}
Topopah Spring Welded	3.57×10^{-18} (1.1)	0.15	5.67×10^{-6}	1.798	0.0801	8.36×10^{-11}
Calico Hills Vitric	1.33×10^{-15} (410)	0.39	1.60×10^{-2}	3.872	0.0405	3.98×10^{-10}
Calico Hills Zeolitic	4.28×10^{-18} (1.3)	0.30	3.08×10^{-3}	1.602	0.1095	2.65×10^{-10}

(1) Average values of samples, Sinnock, Lin, and Brannen, 1984.

(2) Peters et al. (1984), fitted to van Genuchten (1980) formula.

(3) Nimick et al. (1984), Topopah Spring value based on depth-weighted average.

Table 2. Fracture Properties

Unit	Bulk Saturated Permeability (Conductivity [1]) m^2 (mm/yr)	Fracture [2] Spacing D (m) Vertical	Horizontal	Effective [3] Aperture $\bar{b}$ (mm) Vertical	Horizontal	Discrete Fracture [3] Permeability k_g (m^2) Vertical	Horizontal
Tiva Canyon Welded	1.18×10^{-12} (3.65×10^5)	0.17	0.19	0.107	0.111	9.51×10^{-10}	1.02×10^{-9}
Paintbrush Nonwelded	2.43×10^{-13} (7.5×10^4)	1.13	1.40	0.118	0.127	1.16×10^{-9}	1.34×10^{-9}
Topopah Spring Welded	1.18×10^{-12} (3.65×10^5)	0.22	0.48	0.116	0.150	1.12×10^{-9}	1.88×10^{-9}
Calico Hills Vitric	2.43×10^{-13} (7.5×10^4)	1.65	10.	0.134	0.244	1.49×10^{-9}	4.97×10^{-9}
Calico Hills Zeolitic	2.43×10^{-13} (7.5×10^4)	1.65	10.	0.134	0.244	1.49×10^{-9}	4.97×10^{-9}

Unit	Contact[4] Cutoff Aperture b_c (mm) Vertical	Horizontal	Aperture[4] Distribution Parameter β (mm^{-1}) Vertical	Horizontal	Fracture [5] Surface Contact Area ω	Discrete[6] Fracture Compressibility a_v (1/Pa)
Tiva Canyon Welded	0.010	0.011	25.3	24.4	2.8%	1.08×10^{-7}
Paintbrush Nonwelded	0.028	0.030	21.0	19.6	11.8%	9.30×10^{-8}
Topopah Spring Welded	0.028	0.036	21.4	16.5	12%	9.19×10^{-8}
Calico Hills Vitric	0.038	0.069	18.1	9.91	15% (no zeolite)	1.76×10^{-8}
Calico Hills Zeolitic	0.121	0.022	13.8	7.58	50% (include zeolite)	1.76×10^{-8}

(1) Representative values from well J-13, Thordarson (1983); Sinnock, Lin, and Brannen (1984).

(2) Derived from fracture spacings and orientation data in well USW G-4, Spengler and Chornack (1984).

(3) Derived from bulk saturated permeability and fracture spacings, assuming two vertical sets and one horizontal fracture set.

(4) Derived with Gamma distribution from permeability and surface contact area for rough-walled fractures, Wang and Narasimhan (1985).

(5) Assumed to be equal to the fraction of fracture surface coated with clay, calcite and/or zeolite, in well USW G-4, Spengler and Chornack (1984).

(6) $\frac{1}{\phi_f}\frac{d\phi_f}{dP}$, with $\phi_f = \frac{2\bar{b}}{D}$ for two sets of vertical fractures, $\frac{d\phi_f}{dP}$ is measured in core samples with single fractures, Peters et al. (1984).

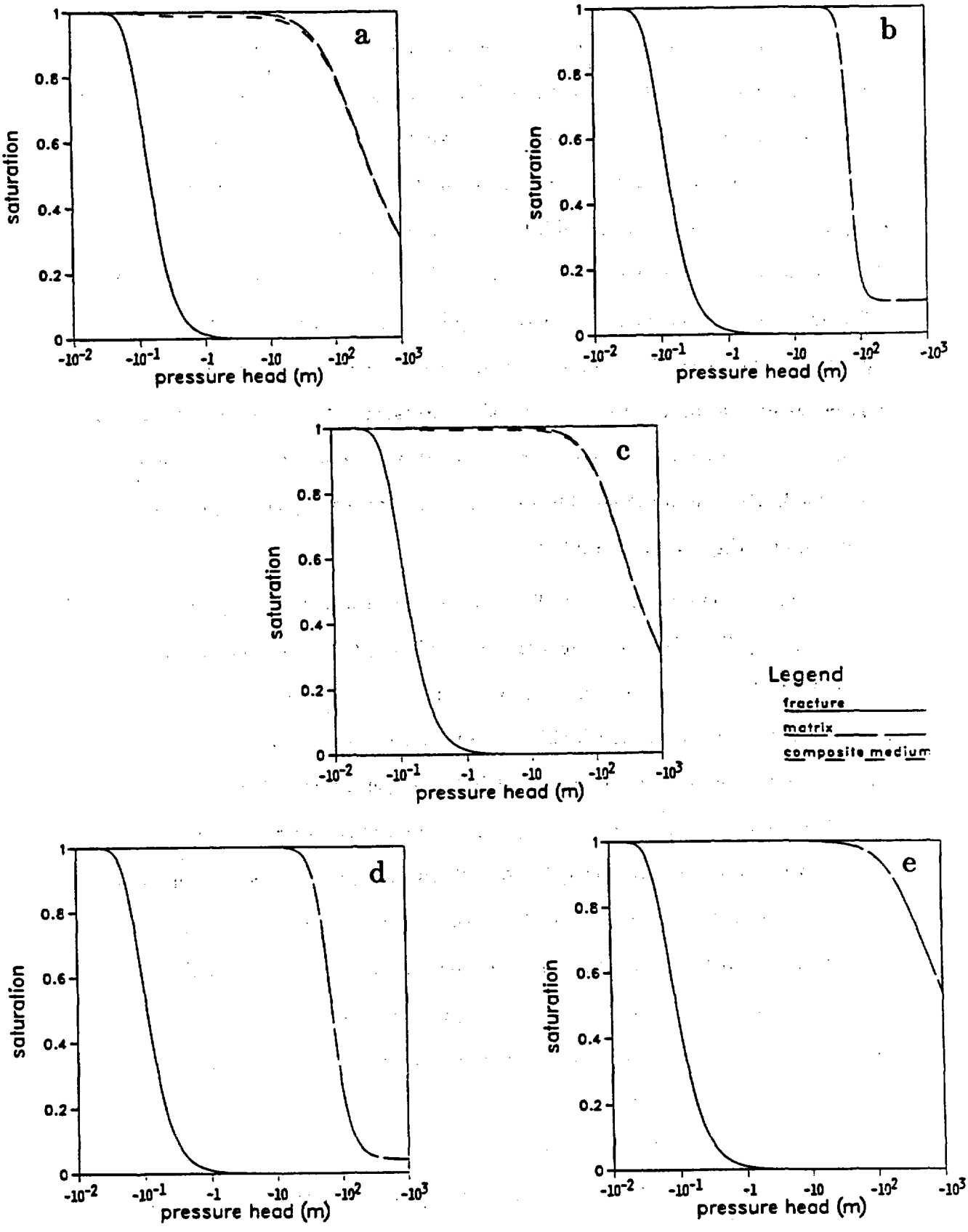

Figure 2. Characteristic Curves of (a) Tiva Canyon Welded Unit; (b) Paintbrush NonWelded Unit; (c) Topopoh Spring Welded Unit; (d) Calico Hills Nonwelded Vitric Unit; and (e) Calico Hills Nonwelded Zeolitic Unit

Figure 3 shows the specific storage capacitances of the discrete fractures and the porous matrix for the five units. The specific storage capacitances represent the volume of water released from a unit volume of tuff per unit change in pressure head. Three physical processes govern the specific storage capacitance: desaturation of pores, compressibility of rock, and compressibility of water (Narasimhan and Witherspoon, 1977). Under partially saturated conditions, the influence of desaturation is orders of magnitude larger than the two compressibility effects. The specific storage capacitances for the fractures peak sharply in a narrow ranges around -0.1 m of suction pressure. The matrix storage capacitances have maximum values around -100 m. The storage capacitances of nonwelded, vitric units (Figs. 3b and 3d) have sharper peaks than the welded or zeolitic units (Figs. 3a, 3c, and 3e).

Figure 4 shows the permeabilities of discrete fractures and porous matrix for the five units. The discrete fracture permeabilities take into account the possibility that liquid flow along the fractures stops when the liquid phase becomes discontinuous (i.e., a 'vapor lock' occurs). This discontinuity, represented by a phase-constriction factor, together with the generalized cubic law relating permeability to aperture, have been used to derive the fracture curves shown in Figure 4 (Wang and Narasimhan, 1985). With the phase-constriction factor, the fracture permeabilities drop from high saturated values to zero at an even smaller suction, about -0.1 m, than the fracture saturation drops shown in Figure 2. The presence of air bubbles in the variable-aperture fracture planes causes effective permeability to become zero even when the saturation of fracture volume is still quite high. With negative pressure, the fractures quickly stop transmitting fluid along the fractures. The water remaining around the fracture contact areas will be quickly sucked into the matrix by capillary forces until the forces in the fractures and in the matrix are equal. This equality will occur when the meniscus

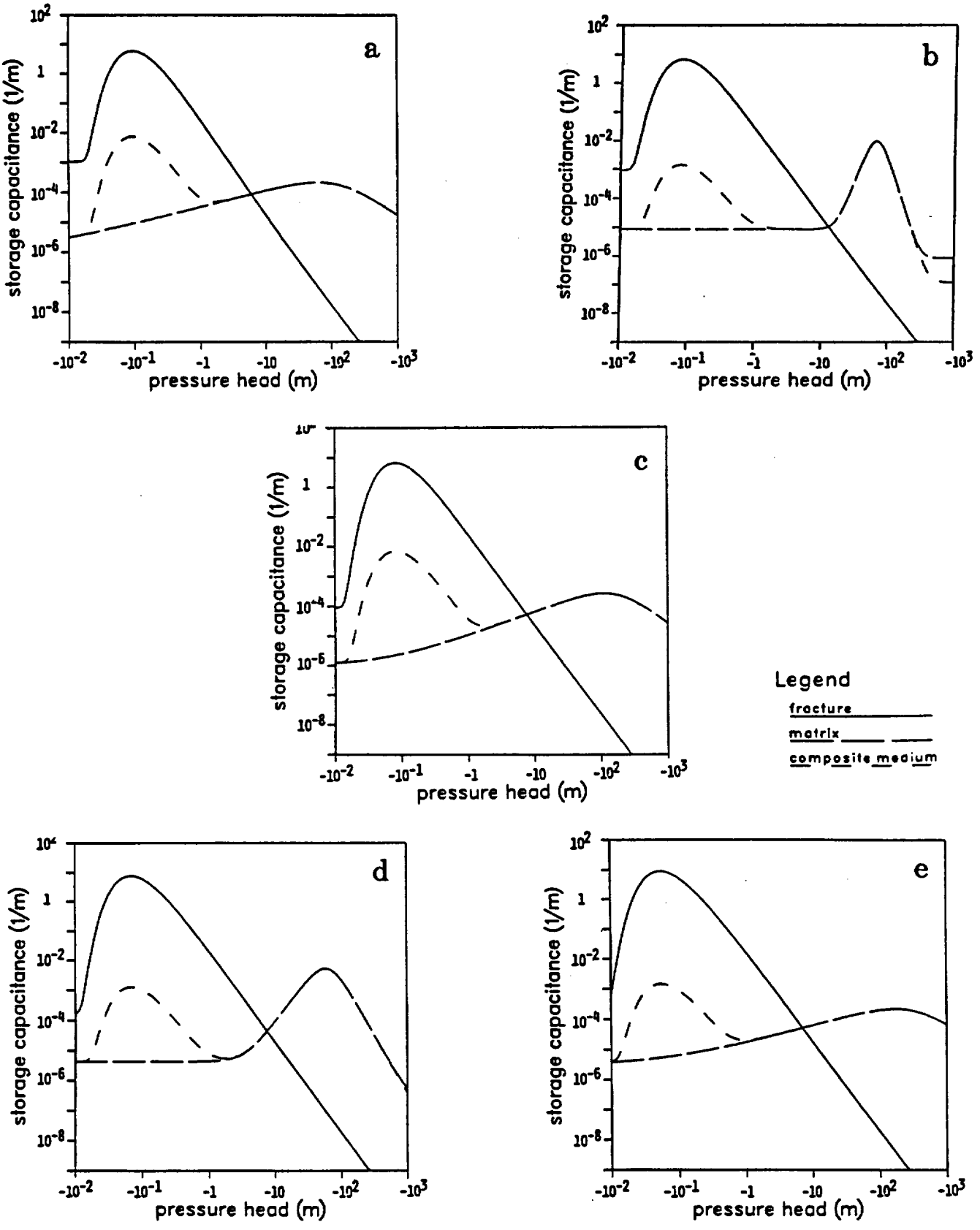

Figure 3. Storage Capacitance of (a) Tiva Canyon Welded Unit; (b) Paintbrush Nonwelded Unit; (c) Topopoh Spring Welded Unit; (d) Calico Hills Nonwelded Vitric Unit; and (e) Calico Hills Nonwelded Zeolitic Unit

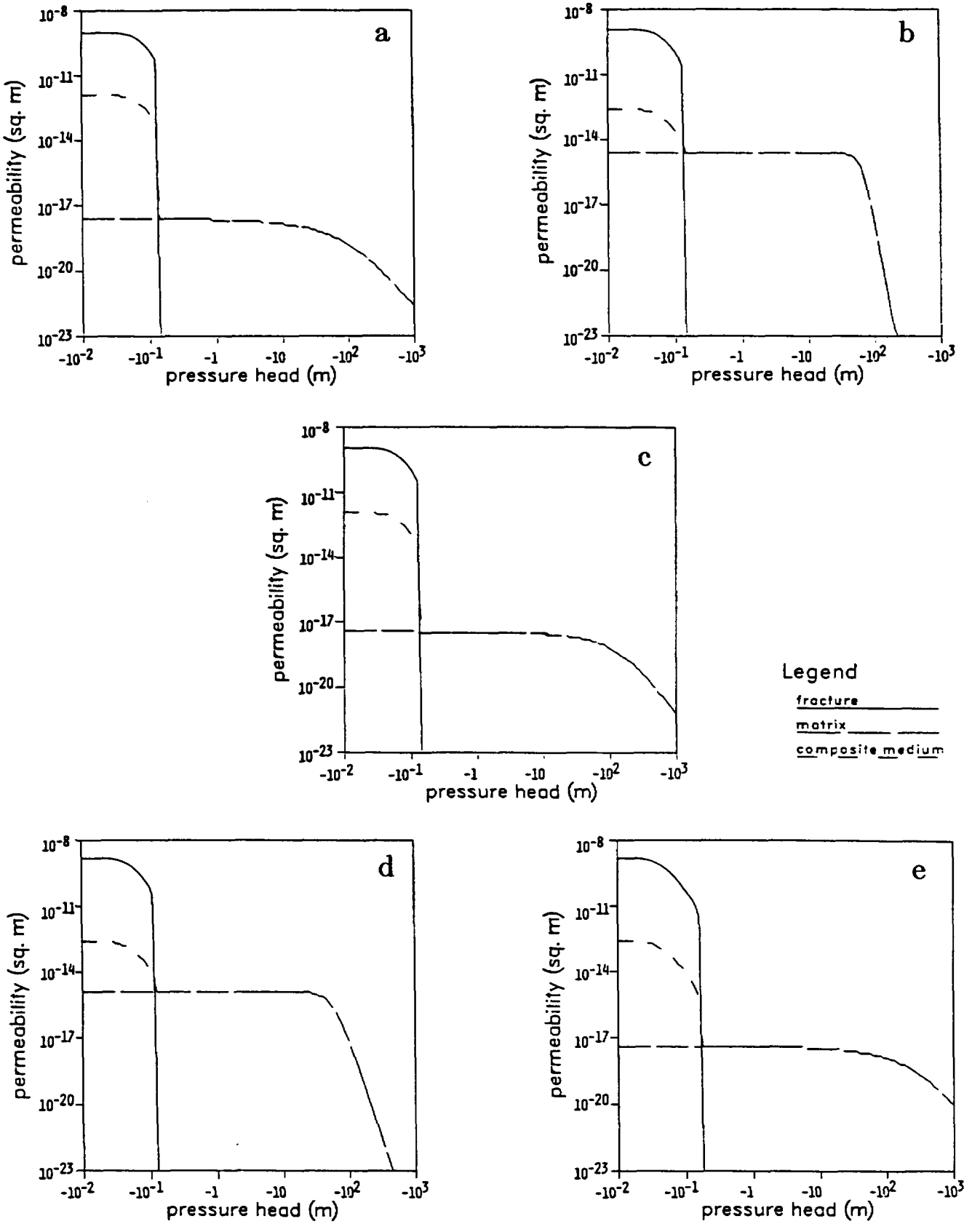

Figure 4. Permeabilities of (a) Tiva Canyon Welded Unit; (b) Paintbrush Nonwelded Unit; (c) Topopoh Spring Welded Unit; (d) Calico Hills Nonwelded Vitric Unit; and (e) Calico Hills Nonwelded Zeolitic Unit

size around the fracture asperities equals the meniscus size in the largest partially saturated pores in the matrix, i.e., when the saturated fracture apertures are within the range of matrix pore sizes. At this point, water in the fractures will behave as a part of the matrix-dominated flow region. Although the saturated matrix permeabilities are much smaller than the saturated fracture permeabilities, especially for the welded and zeolitic units, the tuff matrix in partially saturated conditions will strongly and quickly remove water from the fractures and draw it into the matrix. The flow of water from one matrix block to another will be restricted to the water-wetted contact regions at and around asperities in the fracture planes.

The strong dependencies of both permeability and specific storage capacitance on pressure heads are critical for our understanding of the transient fluid-flow field. It is of interest to note that the hydraulic diffusivity, defined as the ratio of hydraulic conductivity to the specific storage capacitance, changes less abruptly than either the permeability or the specific storage capacitance. The hydraulic diffusivities κ are shown in Figure 5. The region with sharper changes in permeability is also the region with higher storage capacitance associated with desaturation. In the transition region around -0.1 m where the fractures change from highly permeable to nonpermeable flow channels, the matrix diffusivities (stemming from smaller permeabilities and from smaller and smoother storage capacitances) are only slightly smaller than the fracture diffusivities. For systems with properties remaining constant in time, the hydraulic diffusivity (m^2/sec) can be used to estimate the linear penetration depth of perturbations into the flow domains ($\Delta x \approx \sqrt{\kappa t}$, see Carslaw and Jaeger, 1959, for the heat conduction analog). The penetration-depth estimates with different diffusivities can guide mesh design for transient simulations.

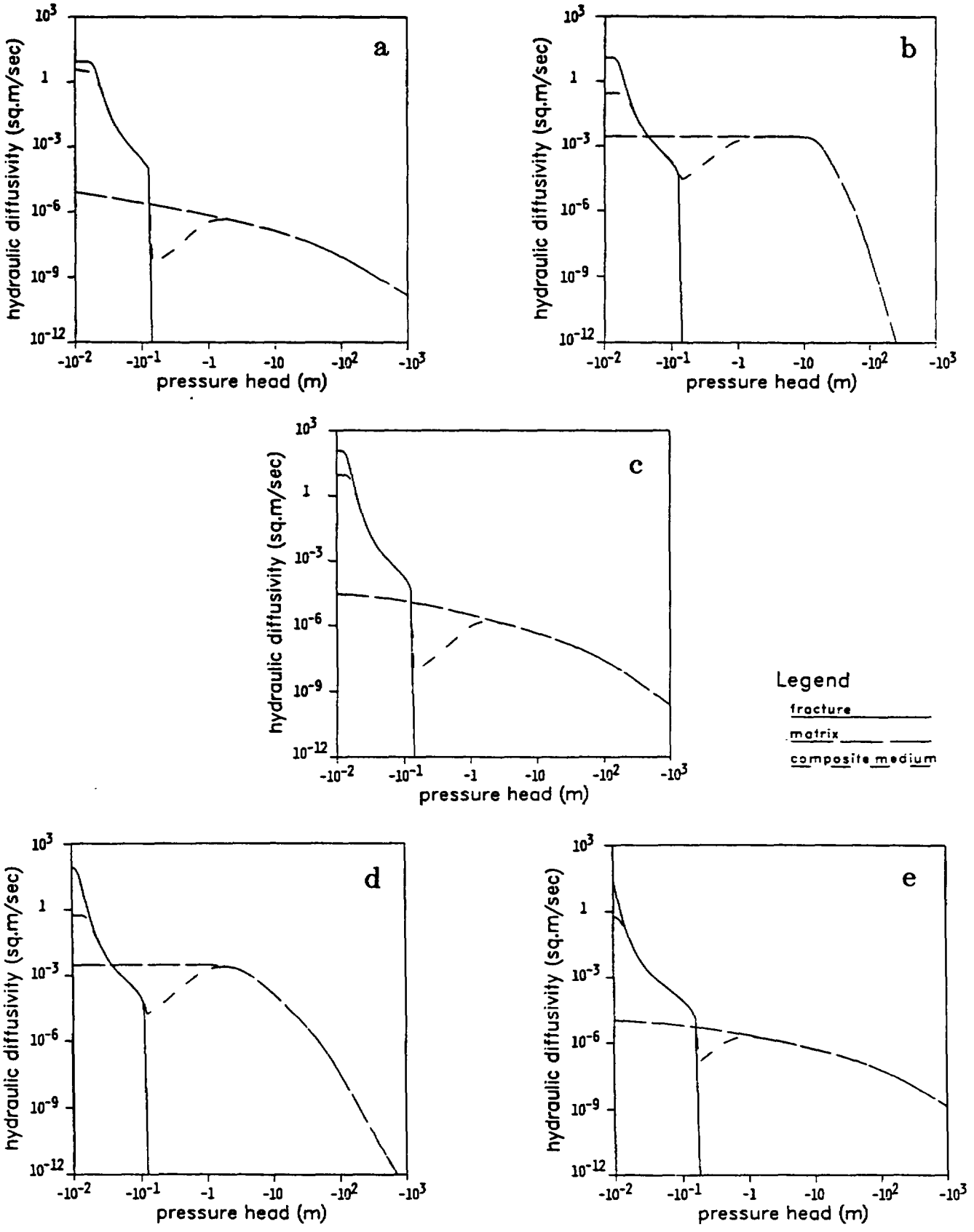

Figure 5. Hydraulic diffusivities of (a) Tiva Canyon Welded Unit; (b) Paintbrush Nonwelded Unit; (c) Topopoh Spring Welded Unit; (d) Calico Hills Nonwelded Vitric Unit; and (e) Calico Hills Nonwelded Zeolitic Unit

Figures 2 through 5 also include the curves for a composite medium model (Klavetter and Peters, 1985; Pruess, Tsang, and Wang, 1984). In a composite-medium model for a fractured porous medium, the permeability is treated as a volume-weighted sum of the fracture permeability and the porous matrix permeability. The contributions of desaturation from the fractures and from the porous matrix to the specific storage capacitances are also additive. The compressibility contributions to the specific storage capacitances are coupled (Klavetter and Peters, 1985). The basic assumption for the composite medium model is that the pressure in the fractures and the pressure in the adjacent porous matrix are equal. Our earlier results (Wang and Narasimhan, 1985) indicate that the pressure in the fractures is essentially the same as the pressure in the matrix when the fractures drain. The additivity of fracture permeability and matrix permeability should be a good approximation in a steady-flow field if the channels of fracture-flow and matrix-flow are parallel. In the transition from fracture-dominated flow near saturated condition to matrix-dominated flow at higher suction pressure, the flow may change from a direction along the fractures to a direction normal to the fracture-matrix interfaces as fluid flows from one matrix block across a fracture to another matrix block.

3.0 Steady-State Infiltration

Yucca Mountain is located in a very arid environment with low precipitation and high evaporation. The net infiltration through the thick, partially saturated units to the deep groundwater table is very low. Direct measurements of net infiltration and recharge have not been made at Yucca Mountain. The saturated hydraulic conductivity of the Topopah Spring welded unit is about 1 mm/yr (see Table 1) and the in situ saturation is 69 $\pm$ 15% (Sinnock, Lin, and Brannen, 1984). The corresponding partially saturated permeability is on the order of 0.5

mm/yr or less, indicating that the most likely upper limit on the amount of flux passing through the Topopah Spring Matrix is probably less than 0.5 mm/yr (Peters, 1984; Sinnock, Lin, and Brannen, 1984; DOE, 1986). From the matric-potential distribution in well USW UZ-1, the water flux in the Topopah Spring welded unit is estimated to be in the range of 0.1 to 0.5 mm/yr (Montazer et al., 1985). The Enviromental Assessment report (DOE, 1986) summarizes various approaches which estimate the net infiltration at Yucca Mountain to be less than a range of about 0.1 to 0.5 mm/yr. Higher net infiltration rates would probably cause steady-state conditions far away from the ambient partially saturated condition. Peters, Gauthier, and Dudley (1985) simulated vertical infiltration and estimated that the Topopah Spring matrix will be nearly saturated and the pressure heads will be nearly zero if the infiltration rate exceeds 0.5 mm/yr. However, some of the net infiltration could be diverted laterally above and below the Topopah Spring unit into a fault zone (Rulon, Bodvarsson, and Montazer, 1985), thereby allowing a flux less than net infiltration to occur at different depths.

Before we present our results for infiltration into partially saturated, fractured porous tuff at Yucca Mountain, it is of interest to briefly review the literature in soil physics on infiltration into heterogeneous systems. For a homogeneous soil, it is well known that if the rainfall intensity is less than the saturated soil conductivity, the soil will tend to attain that uniform saturation at which rainfall intensity exactly matches hydraulic conductivity. If the rainfall intensity exceeds the saturated soil conductivity, ponding of water on the soil surface can occur (Rubin and Steinhart, 1963; Narasimhan and Witherspoon, 1978). If the soil contains macropores such as root channels and worm holes, vertical flow of water into these large cracks or tabular channels occurs only when the rainfall exceeds the infiltration rate into the soil matrix (Beven and Germann, 1982; Edwards et al., 1979; Davidson, 1985). The vertical and horizontal infiltration of

water into a soil matrix can be studied with dye-stained water (Hoogmoed and Bouma, 1980). Scotter and Kanchanasut (1981) used different dyes and different tracers in soil with macropores to show that under partially saturated conditions, the solute flow was much more uniform than in the saturated soil, with tracers migrating through small pores in the soil matrix.

For our heterogeneous fractured, porous tuff units, we also expect that the flow will be in the matrix if the infiltration rate is low and less than the saturated conductivity. With a low infiltration rate, the matrix will be partially saturated and water flow will not occur in the fractures. With matrix-dominated flow, the steady-state flow field can be simulated with explicit fracture-matrix model, composite-medium model, or matrix-only model. We use the TRUST program (Narasimhan et al., 1978) to simulate combinations of these three models in steady-state and transient calculations. The computational grids for the one-dimensional, composite medium calculations are summarized in Table 3 and Figure 6. The thicknesses of the units correspond to the values determined from borehole USW G-4 (Ortiz et al., 1985). The mesh is finer at interfaces between different units, especially at the Paintbrush-Topopah Spring interface for the cases with 0.1 mm/yr. Figure 7 plots the results of steady-state conditions of this infiltration rate. In this report most of our results, exemplified by Figure 7, are presented as plots of vertical profiles of matrix saturation, pressure head, potential, hydraulic conductivity, and Darcy velocity. Computationally, the steady-state conditions were obtained by letting the transient process evolve until changes in conditions are negligibly small. In the final time cycle, the maximum pressure-head change is in the order of 10^{-5} m and all fluxes crossing neighboring nodes agree within 5 significant figures with the infiltration rate at the top of the column. The lowest node is connected to a boundary node maintained at the watertable condition of zero pressure (full saturation). We use a simple, explicit

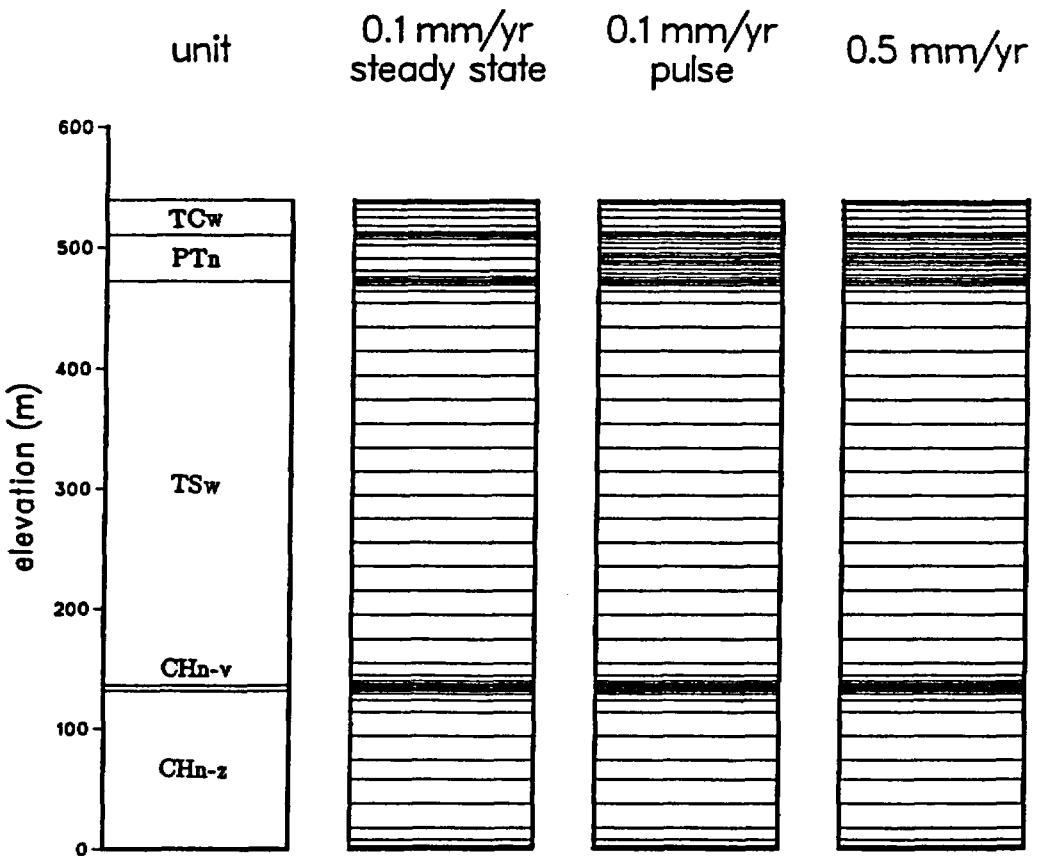

Figure 6. Vertical Grids of Composite Medium Models

integration procedure (see Appendix A, Narasimhan, Alavi, and Tokunaga, 1985) to obtain the initial estimate of pressure distribution and let the TRUST program carry out implicit calculations to obtain the final steady state. The explicit procedure, integrating the Darcy equation node by node from the water table upward to the surface, generally yields good initial estimates of pressure distributions and greatly simplifies the numerical calculation to obtain good final steady-state solutions.

With an infiltration rate of 0.1 mm/yr, the upper part of the Topopah Spring welded unit has a nearly uniform saturation of 80% (Fig. 7a) and constant pressure head of -150 m (Fig. 7b). In the range of constant pressure profile, the pressure gradient is, of course, zero, and the hydraulic potential gradient is unity from the gravity component alone (Fig. 7c). In the range of unit hydraulic gradient, the partially saturated hydraulic conductivity (Fig. 7d) is equal to the Darcy velocity of 0.1 mm/yr (Fig. 7e). Immediately above the Topopah Spring welded unit, the Paintbrush nonwelded unit has a low saturation value (Fig. 7a) and a strongly varying pressure profile, changing from -150 m to -110 m within a few vertical meters (Fig. 7b). The potential gradient is high in this region, dominated by pressure head, although contributions from both pressure gradient and gravity gradient occur (Fig. 7c). This higher gradient compensates for the very low, partially saturated conductivity (Fig. 7d) and maintains the infiltration flux of 0.1 mm/yr. In the upper part of the Paintbrush nonwelded unit, the conductivity approaches the 0.1 mm/yr value, the pressure gradient approaches zero, while the saturation, though increasing, remains low (Fig. 7a).

The profiles of saturation, pressure head, potential, and hydraulic conductivity are sensitive to the infiltration rate. Figure 8 plots the steady-state solutions for an infiltration rate of 0.5 mm/yr. With 0.5 mm/yr, the Topopah Spring welded unit is nearly saturated (Fig. 8a), though the pressure head is still

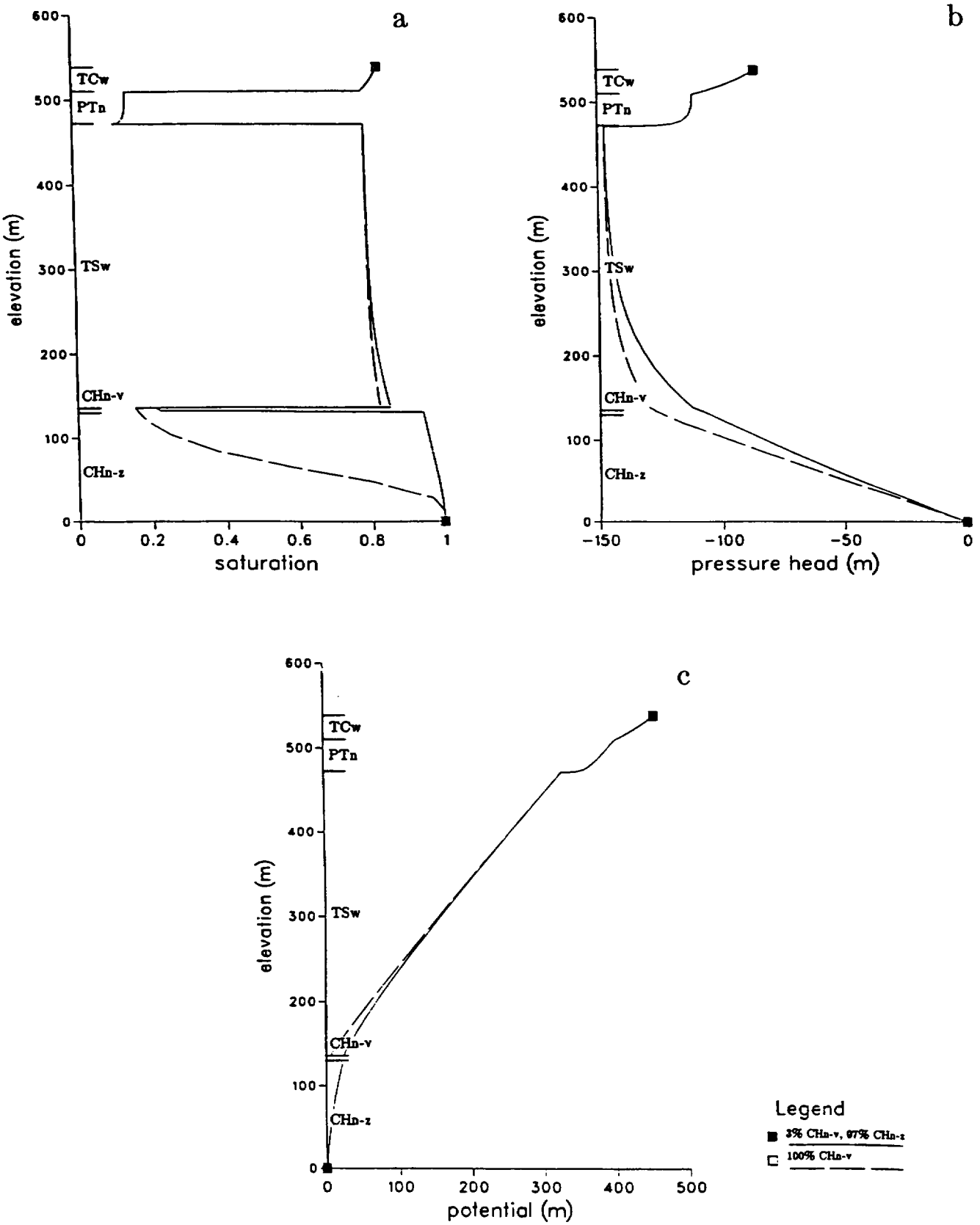

Figure 7. Results for 0.1 mm/yr Steady-State Infiltration

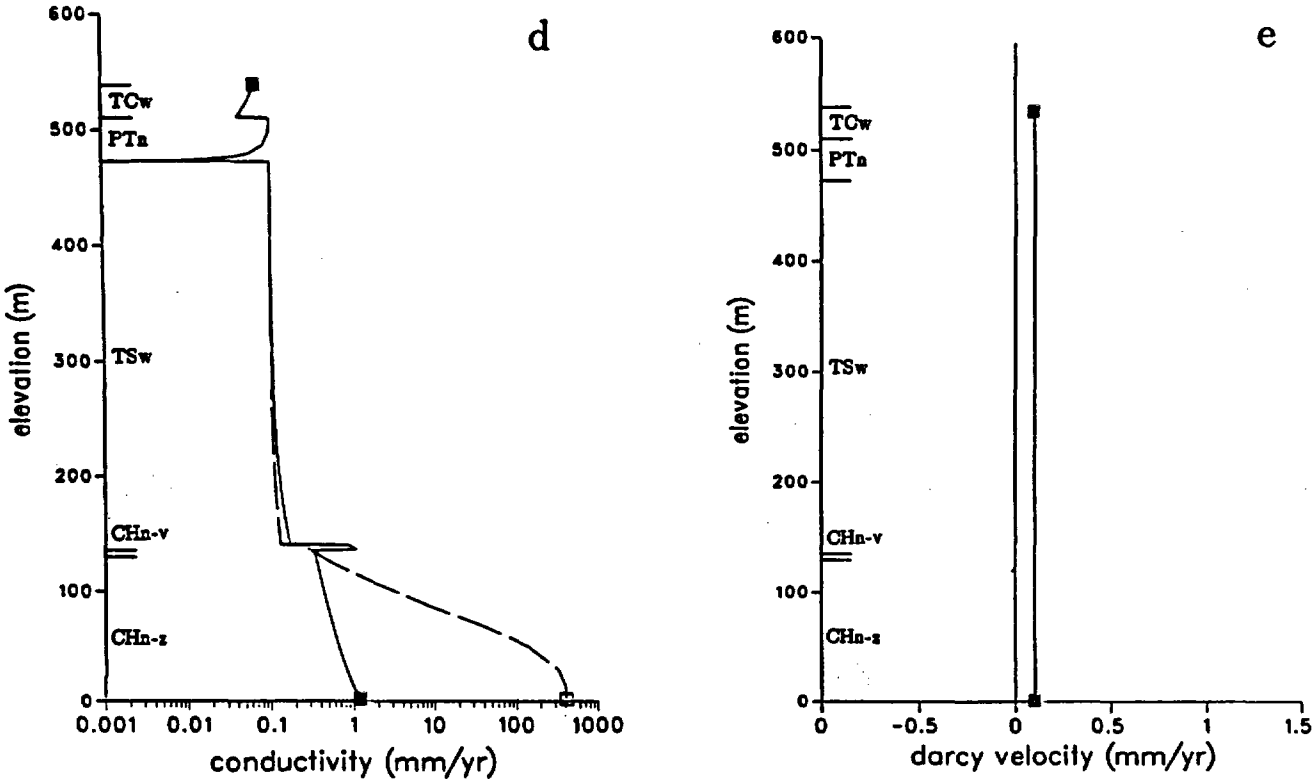

Figure 7. Continued

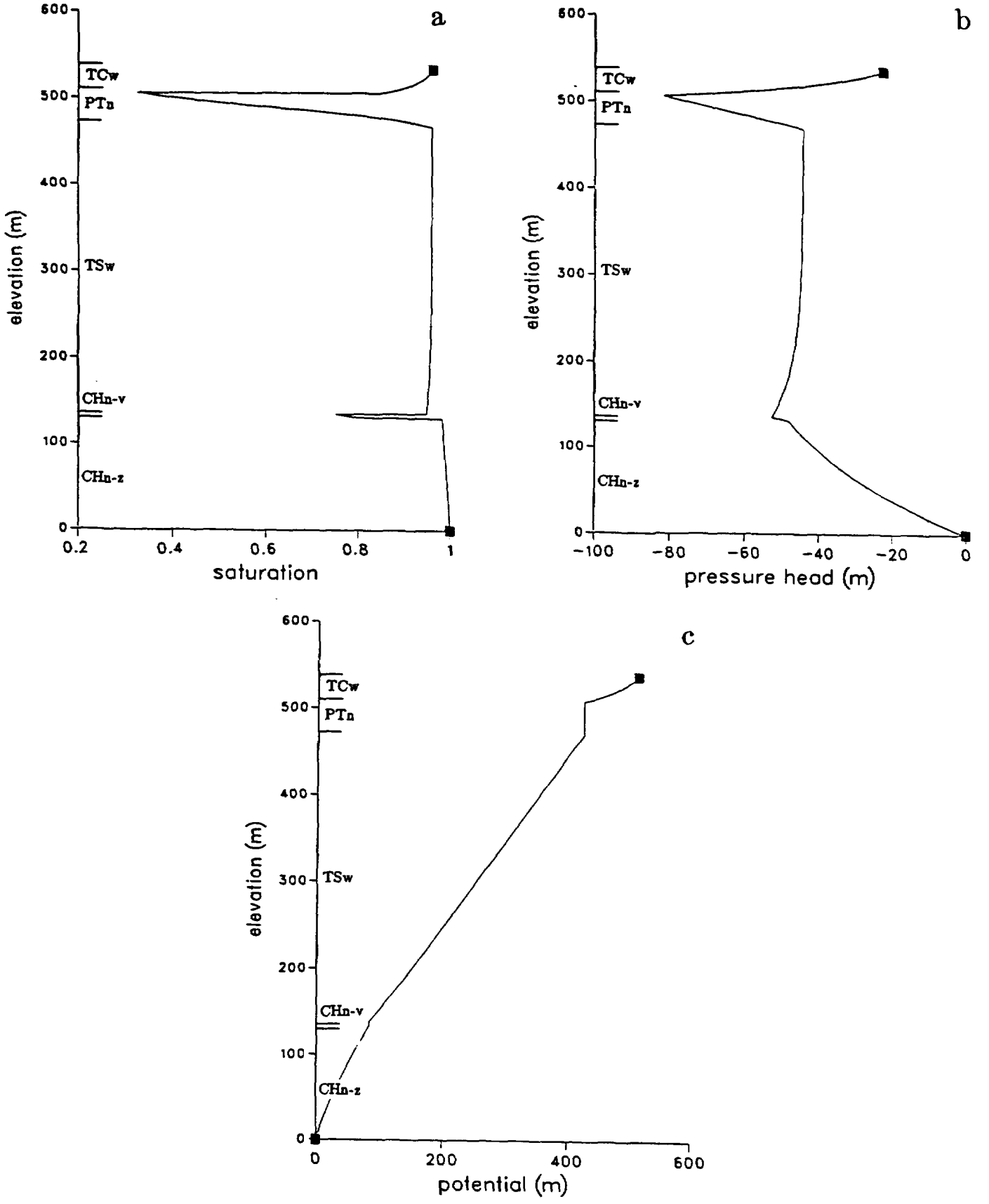

Figure 8. Results for 0.5 mm/yr Steady-State Infiltration

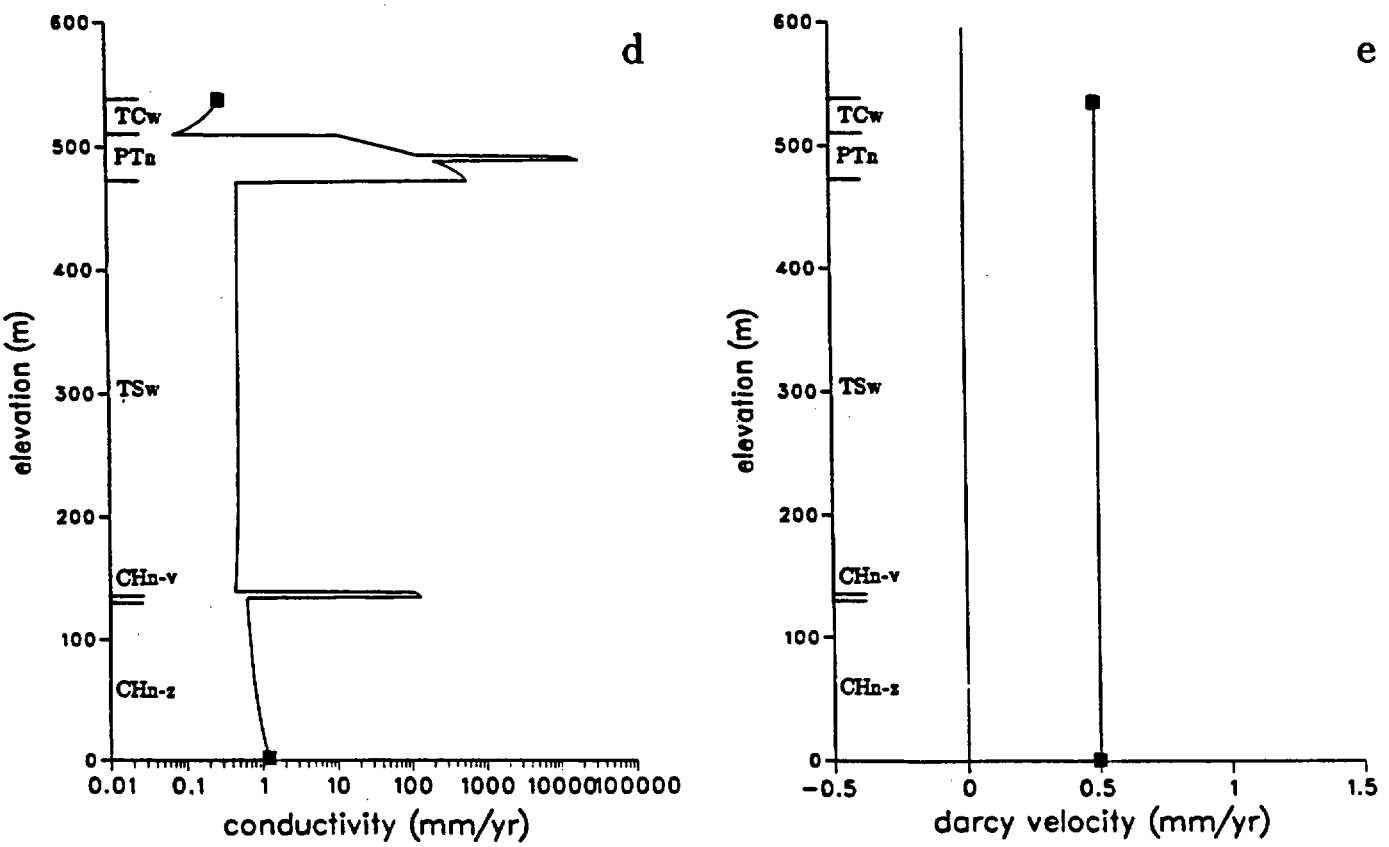

Figure 8. Continued

substantially negative, about -40 m (Fig. 8b). In the Paintbrush nonwelded unit, the pressure head decreases to -80 m, and the potential gradient is extremely small with the pressure-head gradient almost nullifying the gravity gradient (Fig. 8c). In this case, the partially saturated hydraulic conductivity of the Paintbrush unit is much higher than the infiltration flux of 0.5 mm/yr (Fig. 8d). For the 0.5 mm/yr case, the saturated permeability of the middle one-tenth of the Paintbrush nonwelded unit is increased by one-hundred-fold to simulate the possible presence of a high permeability layer. The inclusion of this hypothetical, thin horizontal layer with high permeability does not change the vertical profiles of saturation, pressure head, and potential significantly.

Table 3. Vertical Grid

Unit	Thickness (m)	Grid Spacing (m)		
		0.1 mm/yr Steady State	0.1 mm/yr Pulse	0.5 mm/yr
Tiva Canyon Welded	29.3	1., 2., 5., 6.65, 6.65, 5., 2., 1.		
Paintbrush Nonwelded	38.1	1., 2., 5., 11.05, 10.17, 5., 2., 1., 0.5, 0.2, 0.1, 0.05, 0.02, 0.01	1., 2., 3., 4.15, 4., 2., 1., 1., 1.8, 1., 1., 2., 4., 3.27, 3., 2., 1., 0.5, 0.2, 0.1, 0.05, 0.02, 0.01	1., 2., 3., 4.15., 4., 2., 1., 1., 1.8 1., 1., 2., 4., 4.15 3., 2., 1.
Topopah Spring Welded	335.9	1., 2., 5., 10., 20., 20., 20., 20., 20., 20.,20., 19.9, 20., 20., 20., 20., 20., 20., 20., 10., 5.,2., 1.		
Calico Hills Vitric	4.6	1., 1.3, 1.3, 1.		
Calico Hills Zeolitic	131.7	1., 2., 5., 10., 20., 20., 15.7, 20.,20.,10., 5., 2., 1.		

The differences in the results between the 0.1 mm/yr case and the 0.5 mm/yr case in the Paintbrush nonwelded unit can be understood by analyzing the characteristic curves (Figs. 2b and 4b). At the Topopah-Paintbrush interface, with -150 m suction in the 0.1 mm/yr case, the Paintbrush nonwelded unit is almost completely desaturated, and the hydraulic conductivity is nearly zero. To allow water pass, the pressure head in the unit rapidly increases upward over a few meters of elevation to -110 m, simultaneously providing a strong hydraulic gradient at the interface as well as an increase of hydraulic conductivity. However, in the 0.5 mm/yr case, the pressure head at the Topopah-Paintbrush interface is -40 m, and the corresponding hydraulic conductivity of the Paintbrush is much greater than 0.5 mm/yr. Hence, only an extremely small hydraulic gradient is needed to pass 0.5 mm/yr through the Paintbrush unit.

Below the Topopah Spring is the Calico Hills nonwelded formation, which is vitric in the upper part and is zeolitic in the lower part. Figure 7 for the 0.1 mm/yr case also includes the simulation results, assuming the Calico Hills nonwelded unit is completely vitric. These results demonstrate that the steady-state profiles in the upper layers are insensitive to conditions in the lower layers for the 0.1 mm/yr case. The relative thicknesses of the vitric and zeolitic units vary throughout the mountain. At well USW G-4, the vitric unit is very thin (4.6 m or 3% of the total unsaturated Calico Hills thickness, Ortiz et al., 1985). Hydrologically, a distinct vitric unit may be absent at well USW G-4 with the saturated permeability of this unit having a value closer to one characteristic of the underlying zeolitic unit (Peters, personal communication, 1985). We use the saturated permeability value in Table 1 (Sinnock, Lin, and Brannen, 1984) for this thin vitric unit to simulate the possible presence of a layered, low-high-low permeability sequence below the Topopah Spring unit. In other locations, such as at well USW GU-3 in the southern tip of Yucca Mountain, the zeolitic unit is

missing (Ortiz et al., 1985). Figure 7 compares the results assuming 3% vitric and 100% vitric. The insensitivity of the profiles of pressure head and saturation in the upper units to the profiles in the lower units suggests that we may approximately decouple the upper interface studies from those of the lower parts for the 0.1 mm/yr case. The simulations in the next section will use this approximation. The thick Topopah Spring unit damps out the boundary effects from both the upper and the lower boundaries. The solution in the Topopah Spring unit is essentially determined by demanding the saturation to attain an uniform value at which the infiltration rate exactly matches the partially saturated, effective hydraulic conductivity.

4.0 Pulse Infiltration Through Upper Units

In this section, we discuss the responses of the fractured, porous units to infiltration pulses of high rates and short durations. We will focus on the upper layers in Yucca Mountain. Capillary theory, various modeling studies, and experimental evidence in soil sciences all strongly support a conclusion that the fluid flow is mainly through the tuff matrix if the net infiltration rate is less than the saturated conductivity of the matrix. However, we would still like to investigate possible scenarios whereby the fractures might contribute to fluid flow when infiltration is not constant in time and when short-term pulses with rates much higher than the saturated matrix conductivity occur periodically.

To focus on the upper units, we choose for detailed analysis a vertical section with 10 m of Tiva Canyon welded unit on the top, the whole 38.1 m of the Paintbrush nonwelded unit in the middle, and 10 m of Topopah Spring welded unit on the bottom. In the analysis, we use a discrete fracture-porous matrix model as well as a composite medium model. The discrete model for the welded units (Table 4 and Figure 9) contains both vertical fracture grids and horizontal

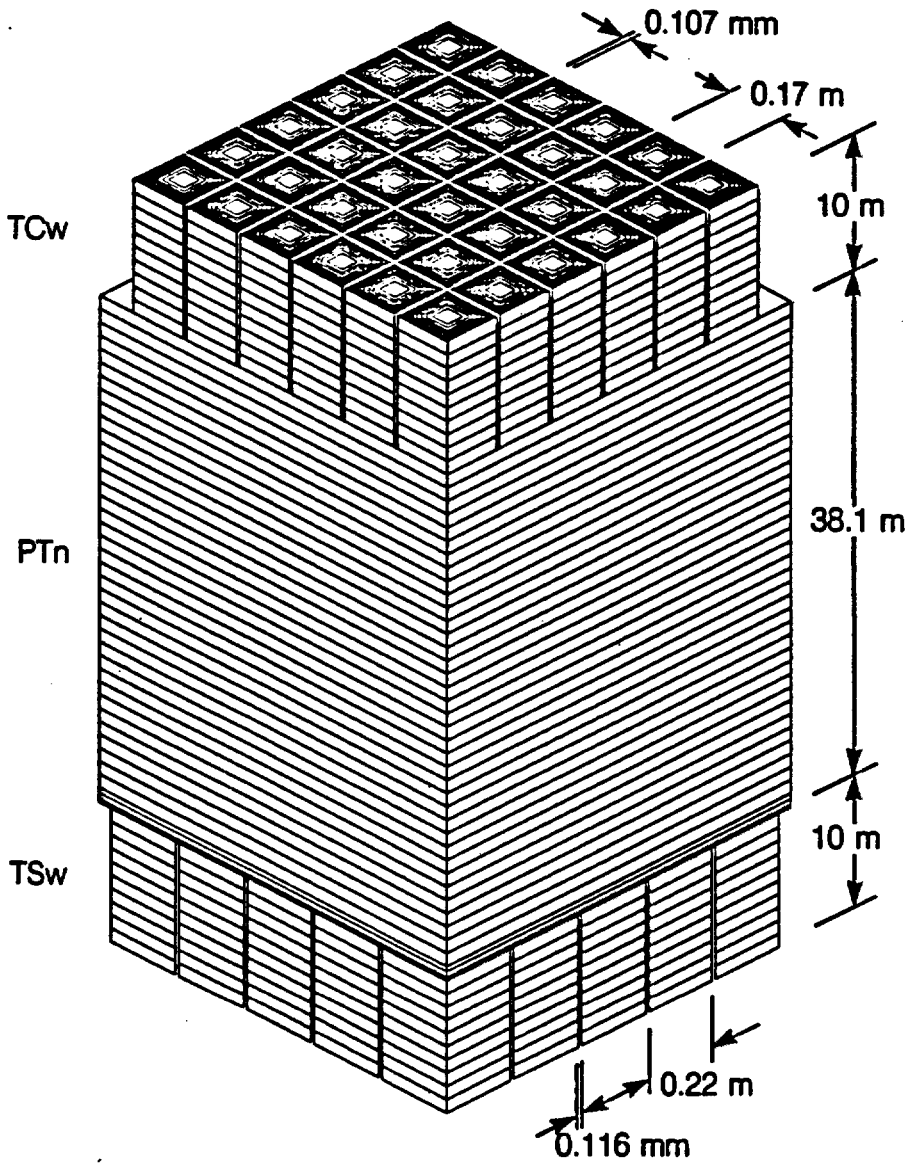

Figure 9. Multiple Interacting Continuum Grids of Discrete Fracture and Porous Matrix Models

connections from the vertical fractures into the matrix. Each matrix block is partitioned into 10 nested, equal-volume continua, idealized with the multiple interacting continuum (MINC) mesh generator (Pruess and Narasimhan, 1985). Vertically, the matrix continua of neighboring nodes are directly connected. For the vertical infiltration problem, we take into account only two orthogonal vertical fracture sets. Earlier studies, with both vertical and horizontal fractures explicitly modeled, indicated that horizontal fractures did not significantly affect the vertical flow rate (Wang and Narasimhan, 1985). For the Paintbrush nonwelded unit, the fracture spacings are much larger than the welded units. For most steady-state and transient-pulse cases, the fluid flow field in the Paintbrush nonwelded unit is dominated by matrix flow. We can either neglect the fractures in the nonwelded unit or treat the nonwelded unit as a composite medium. These two treatments yield essentially the same results. The fracture continua and the matrix continua of the welded units are connected to the grid blocks of the nonwelded unit.

Table 4. Fracture-Matrix Grid

Unit	Vertical Thickness (m)	Horizontal Thickness* (mm)
Tiva Canyon Welded	ten 1.'s	0.053, 4.4, 4.7, 5.0, 5.3, 5.8, 6.4, 7.2, 8.3, 11.2, 13.6
Paintbrush Nonwelded	thirty-seven 1.'s 0.4, 0.4, 0.2, 0.1	
Topopah Spring Welded	ten 1.'s	0.058, 5.7, 6.0, 6.4, 6.8, 7.4, 8.2, 9.3, 11.1, 14.4, 17.4

*First node is for the fracture continuum, next 10 nodes are for the matrix continuum.

For simulations involving infiltration pulses, the initial conditions correspond to the steady-state solution with a constant infiltration source of 0.1 mm/yr on the top Tiva Canyon welded unit node and a sink of 0.1 mm/yr on the bottom Topopah Spring welded unit node. The infiltration pulses are applied to the fracture continuum at the top. To systematically study this problem, first we fix the duration of pulse to 0.2 yr, corresponding to an intense rainfall or snow melt period. The pulses are applied periodically. The periods are chosen to be 1 yr, 5 yr, 50 yr, 500 yr, and 5,000 yr. For the 1-yr pulse, the intensity of the infiltration is 0.5 mm/yr, which corresponds to 1 yr x 0.1 mm/yr, divided by 0.2 yr. For the 5,000-yr pulse, the intensity of infiltration is 2,500 mm/yr, which corresponds to 5,000 yr x 0.1 mm/yr, divided by 0.2 yr. For the case with 5,000-yr pulse, all the infiltration in 5,000 yr is applied to the system within 0.2 yr. After 0.2 yr, the infiltration rate is zero until the start of the next infiltration pulse, 4999.8 yr later. The average infiltration rate over any 5,000-yr period is the same as the constant infiltration rate of the initial steady-state condition.

For the mild and frequent pulses (1 yr, 5 yr, and 50 yr), the matrix was found to always remain partially saturated and the fractures essentially dry. Figure 10 shows the results for the 1-yr and 5-yr infiltration pulses for the duration of one cycle, i.e., from the onset of one infiltration event until the onset of the next. The effects of the pulses are completely damped out in the Tiva Canyon welded unit. These results are consistent with the findings of Travis et al. (1984) that a slug of water moving through fractures with apertures as small as 0.1 mm will be unable to penetrate more than a few meters, at most, through fractured welded tuff with matrix saturations as high as 90%. Repeated pulsing does not change the capacity of the partially saturated matrix of the Tiva Canyon welded unit to absorb all the pulsed water by capillarity. Even for a 50-yr pulse with many cycles of repeat pulsing (Fig. 11), the transient changes are limited within

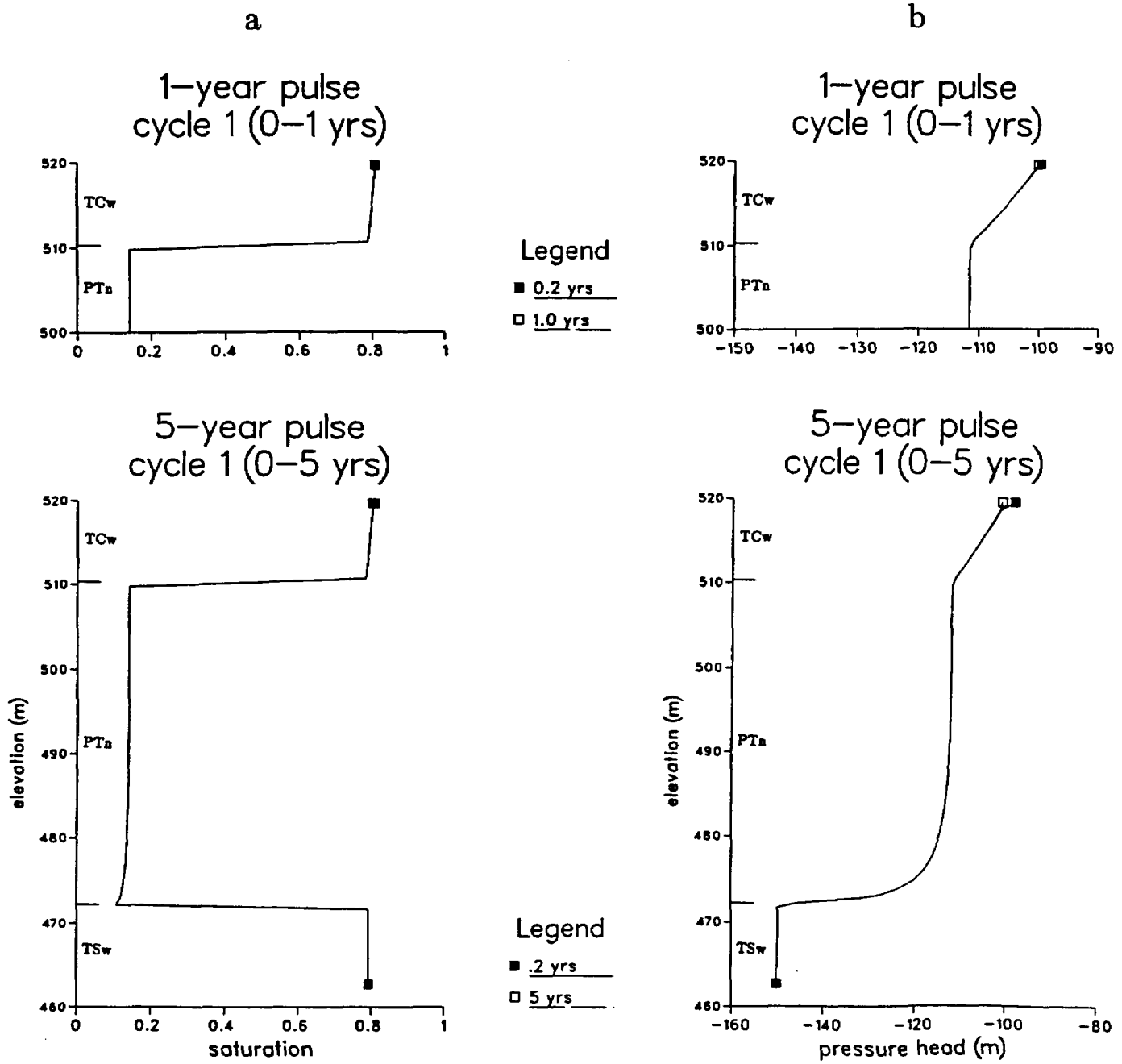

Figure 10. Results for 1-yr and 5-yr x 0.1 mm/yr Transient- Pulse Infiltration

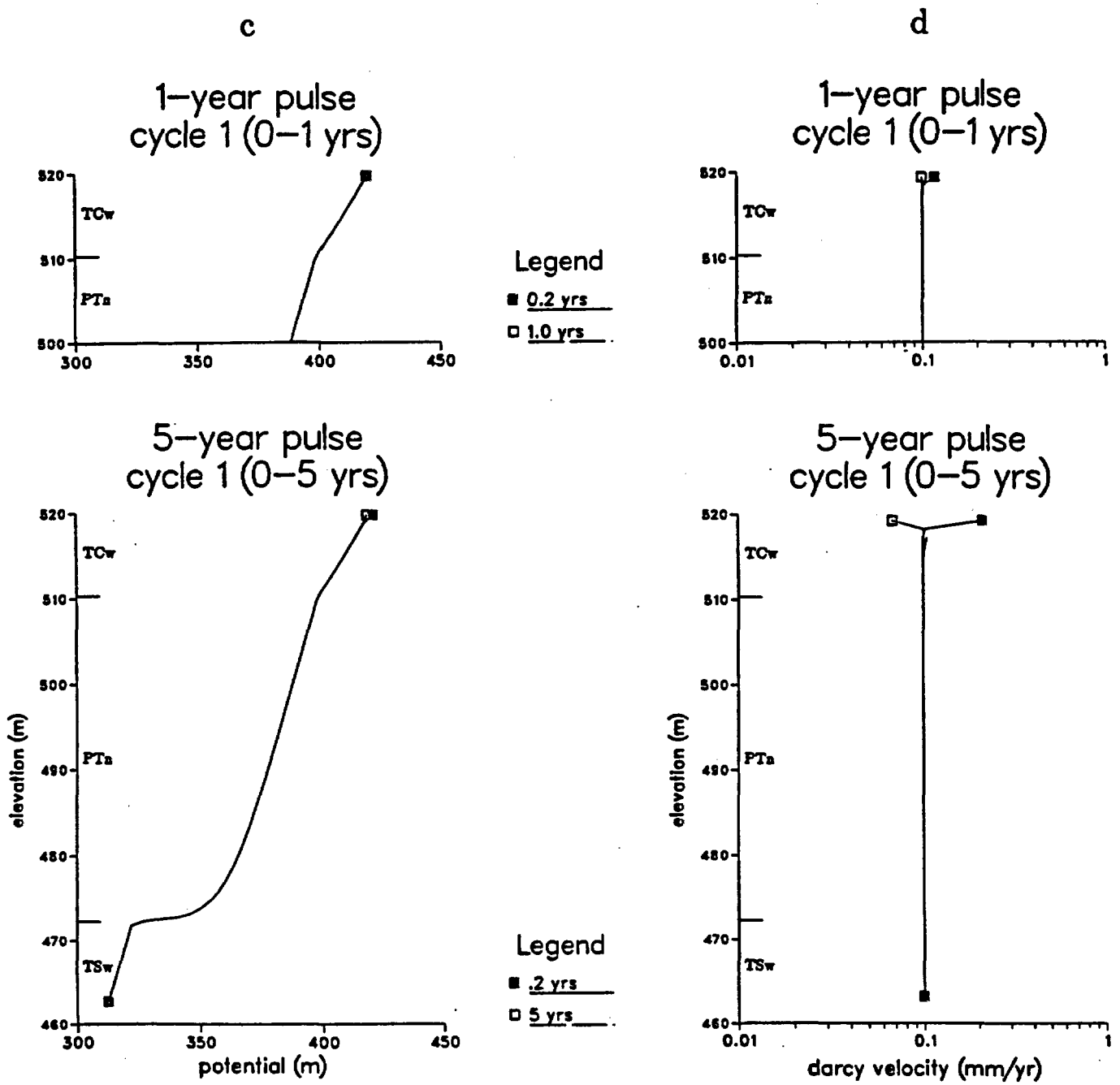

Figure 10. Continued

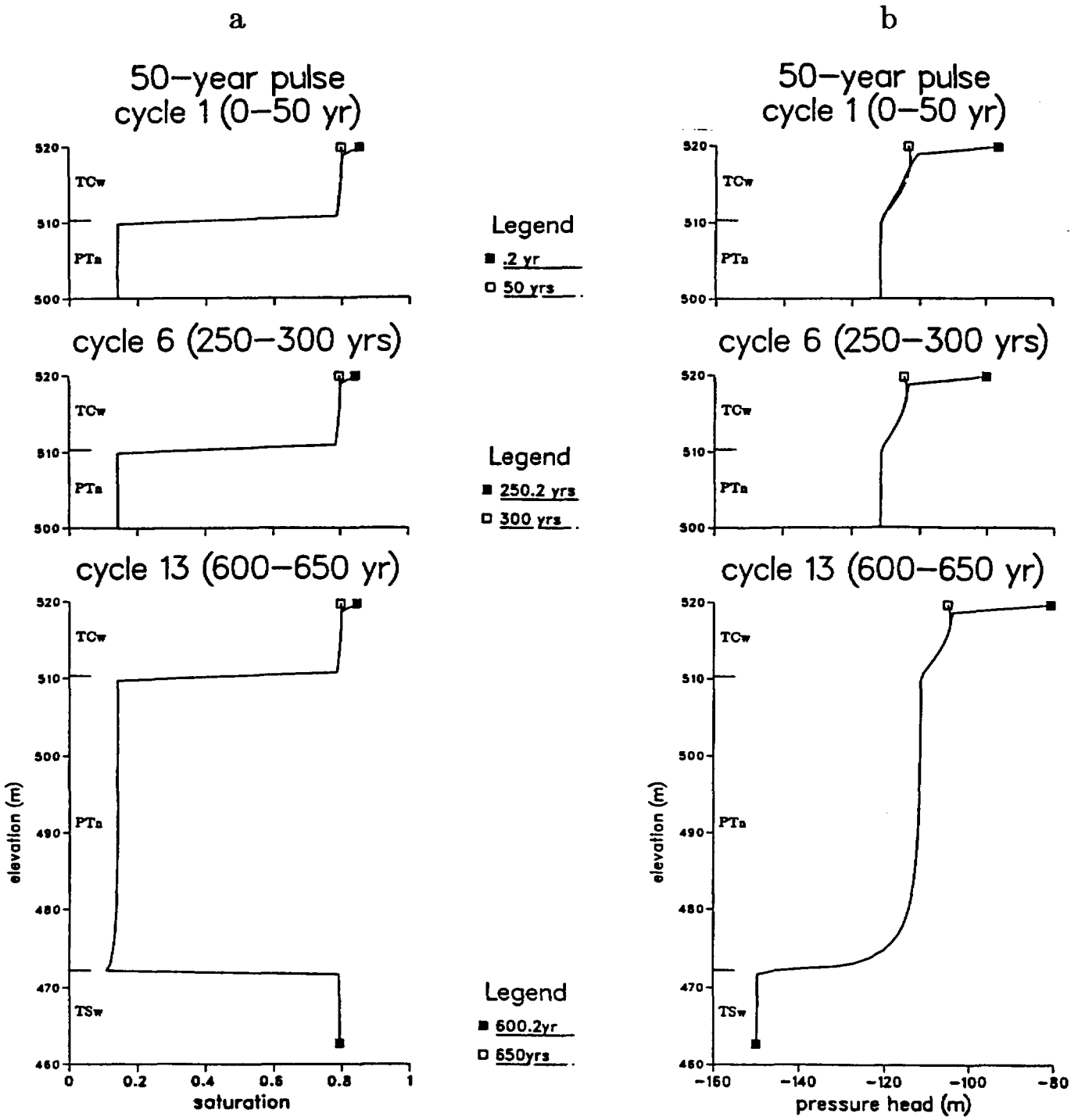

Figure 11. Results for 50-yr x 0.1 mm/yr Transient-Pulse Infiltration

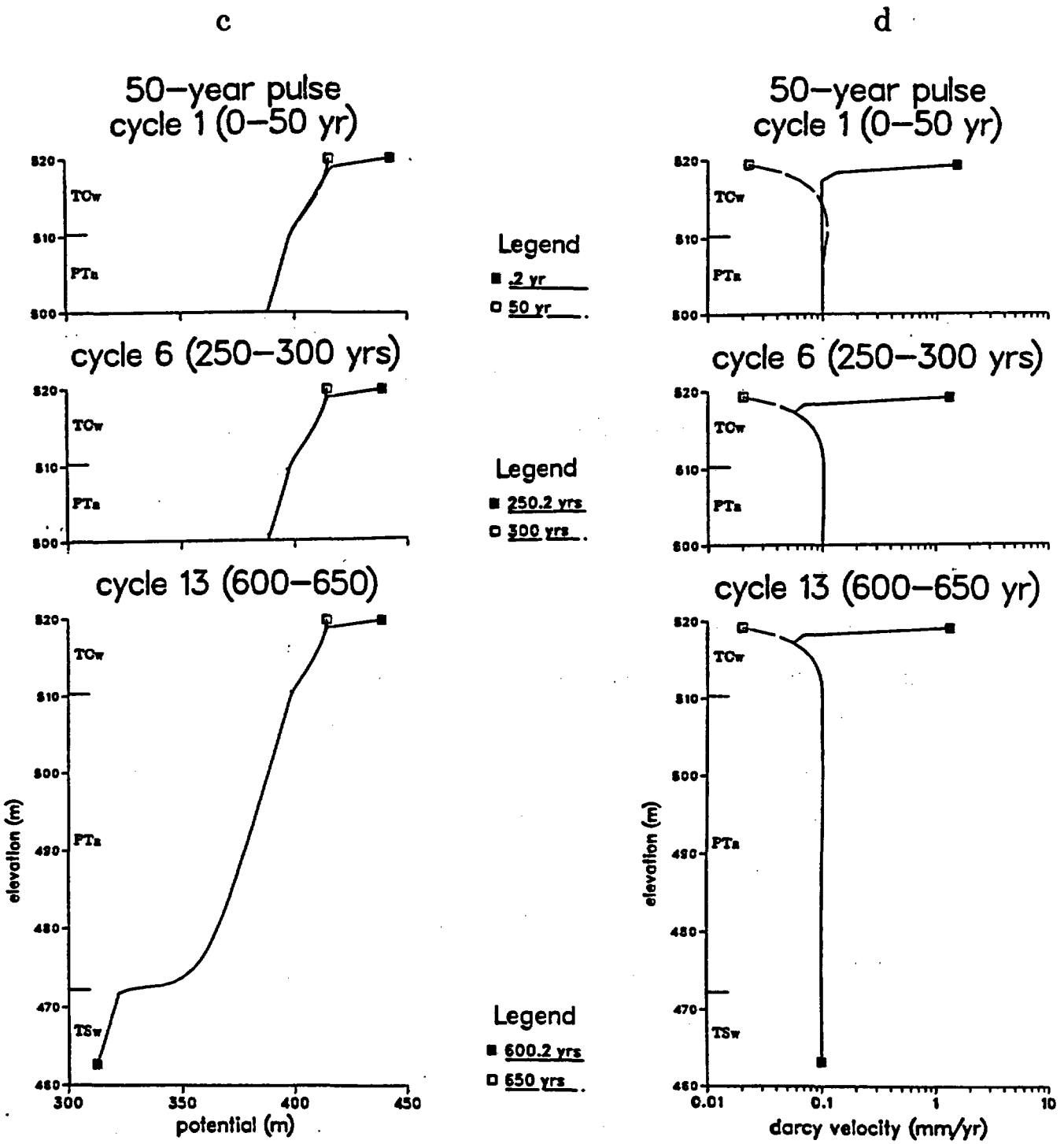

Figure 11. Continued

the Tiva Canyon welded unit and the matrix remains partially saturated.

For the 500-yr pulse, the intensity of the infiltration pulse (250 mm/yr for 0.2 yr) is high enough to saturate the top 2 m of the Tiva Canyon welded unit. Figure 12 illustrates the horizontal saturation profiles within the topmost matrix block of the Tiva Canyon welded tuff. The pulse is applied to vertical fractures surrounding the matrix block. At time t=0, the first (topmost) discrete fracture continuum node starts to receive all the water at a rate corresponding to 250 mm/yr infiltration per unit surface area. Although the water enters the fracture node first, it does not accumulate in the fractures which remain partially saturated. The water is quickly sucked into the matrix and distributed nearly evenly throughout the matrix block, which is simulated with 10 nested nodes. The matrix saturations near the matrix-fracture interfaces, 0.085 m or half the vertical fracture spacing of Tiva Canyon welded unit (see Table 2) away from the matrix block center, are only slightly higher than the matrix saturations in the center of the matrix block. At t=0.08 yr, the matrix block becomes fully saturated (S=1). The total amount of water infiltrated from t=0 to t=0.08 yr is approximately equal to the initial available pore spaces, $\phi(1-S)$, in the topmost matrix block. For the Tiva Canyon welded unit with porosity of $\phi=0.1$ and an initial saturation of S=0.8 (Fig. 7a), the available pore space in the 1-m-thick block will be filled in 0.1 x (1 - 0.8) x 1 m divided by 250 mm/yr, or 0.08 yr. As the matrix approaches full saturation and the negative pressure head approaches zero, the saturation in the fractures increases and water moves down through fractures to the next fracture node. The process of horizontal wetting of the second matrix block follows essentially the same fast-suction, even-wetting behavior of the first matrix block shown in Figure 12. Since we can calculate the times required for each block to become fully saturated by the available pore volume and the intensity of pulse without detailed calculations of the horizontal

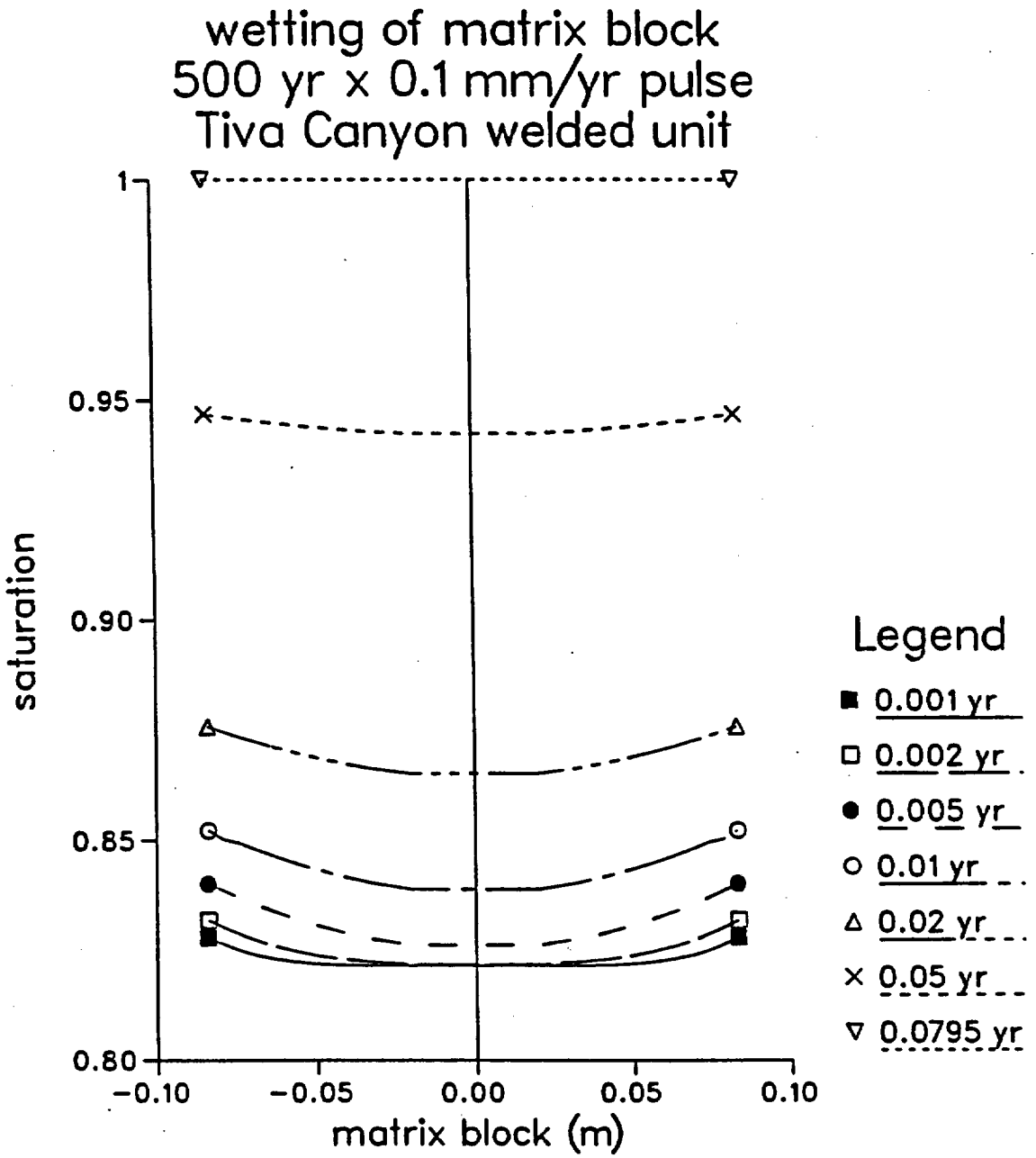

Figure 12. Horizontal Saturation Profiles Within the Top Matrix Block in Response to Infiltration of Water in the Fractures Surrounding the Matrix Block

wetting and vertical sharp wetting front movements, we use the following procedure to simplify the pulse calculations. As each block from the top downward becomes fully saturated, we apply the pulse to the fracture just below the block. For the 500-yr pulse, the first 2 m of Tiva Canyon welded unit will be saturated in 0.16 yr, and we apply 250 mm/yr at the third block from the top for the remaining 0.04 yr to complete the 0.2-yr pulse period. After the pulse period, the infiltration stops and the fractured, porous medium evolves as water redistributes through the matrix under capillary and gravitational forces. With this treatment, we approximate the sharp front movements and model the responses of the system to high-intensity, transient pulses.

The results for the first cycle for a 500-yr pulse are shown in Figure 13. Changes in saturation, pressure, potential, conductivity, and Darcy velocity occur mainly in the 10 m section in the Tiva Canyon welded unit. Full saturation occurs only in the upper part of Tiva Canyon welded unit during the infiltration period. The pulse effects penetrate slightly into the upper part of the Paintbrush nonwelded unit but do not reach the Topopah Spring welded unit. Effects of a second cycle (Fig. 14) are similiar to those of the first cycle (Fig. 13). For a 5,000-yr pulse (Figs. 15 and 16), the 10 m section of the Tiva Canyon welded unit is completely saturated during the infiltration period. After infiltration of 2,500 mm/yr over 0.2 yr, the infiltrating water moves through the Paintbrush nonwelded unit and reaches the Topopah Spring welded unit in about 1,000 yr. Even for this large pulse, the Paintbrush nonwelded unit and the Topopah Spring welded unit remain partially saturated. Since the 5,000-yr pulse effects do reach the Topopah Spring welded unit, one may question if the lower boundary used in the simulations was perhaps too close to the Topopah-Paintbrush interface. We further discuss the 5,000-yr pulse simulations using an extended grid after we discuss the lateral flow.

5.0 Lateral Flow

The stratigraphic units at Yucca Mountain generally tilt eastward at 5 ° to 7 ° (Scott and Bonk, 1984). Several Investigations have suggested that a horizontal vector of the gravity gradient caused by the tilt may divert some of the water laterally to a high-conductivity fault zone where vertical flow of the diverted water can continue (Montazer and Wilson, 1984; Rulon, Bodvarsson, and Montazer, 1984). If the hydraulic conductivity of the nonwelded units is anisotropic and the material properties along fault zone can accommodate large, partially saturated flow downward to the water table, then lateral flow through the nonwelded units could divert a substantial fraction of net infiltration away from dispersed vertical flows through the welded units to concentrated vertical flow through localized fault zone. On the other hand, if the magnitude of lateral flow is much larger than the capacity of the fault zone to transmit water downward, then ponding (local perched zones of saturation) may occur in the eastern part of the nonwelded units. This would create a saturation gradient acting against the lateral component of the gravity gradient. In this report, we ignore the potential effects of fault zones and ponding. Instead, we roughly estimate the potential for and magnitude of lateral flow using a fixed-gradient approximation.

In the fixed-gradient approximation, each node in the nonwelded units is allowed to leak water laterally. The magnitude of the leakage flux from each node is the product of the partially saturated hydraulic conductivity, the lateral component of the gravity gradient, and the area of cross section on the east side of the grid block. We chose a fixed lateral gradient of 6%, corresponding to the average slope of the rock units. The total cross sectional area on the east side of the Paintbrush nonwelded unit is 38.1 m thickness times the unit width. The partially saturated conductivity values for each node are determined by the pressure values for each node. This approximation is used in both the steady-state

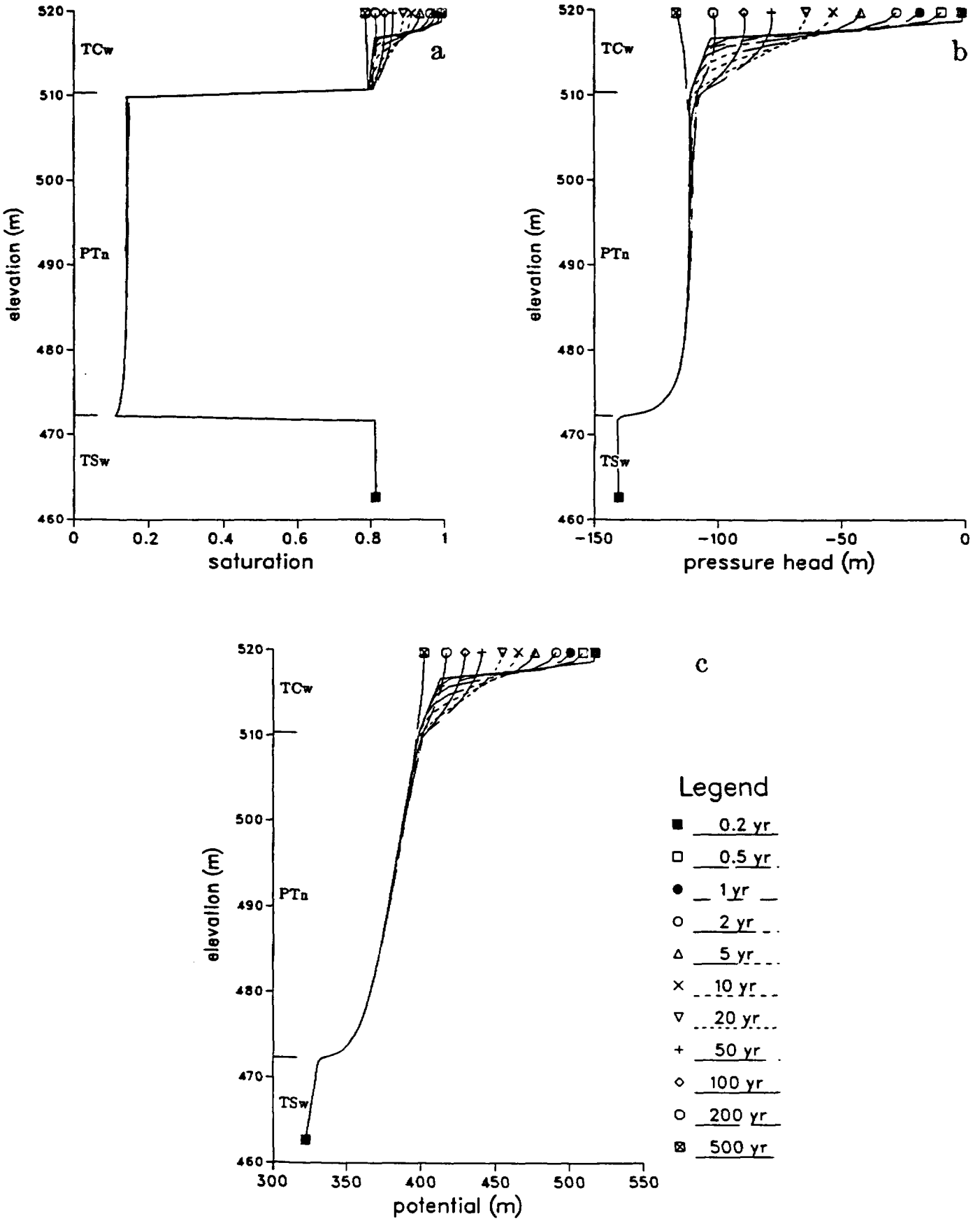

Figure 13. Results for the First Cycle of 500-yr x 0.1 mm/yr Transient-Pulse Infiltration

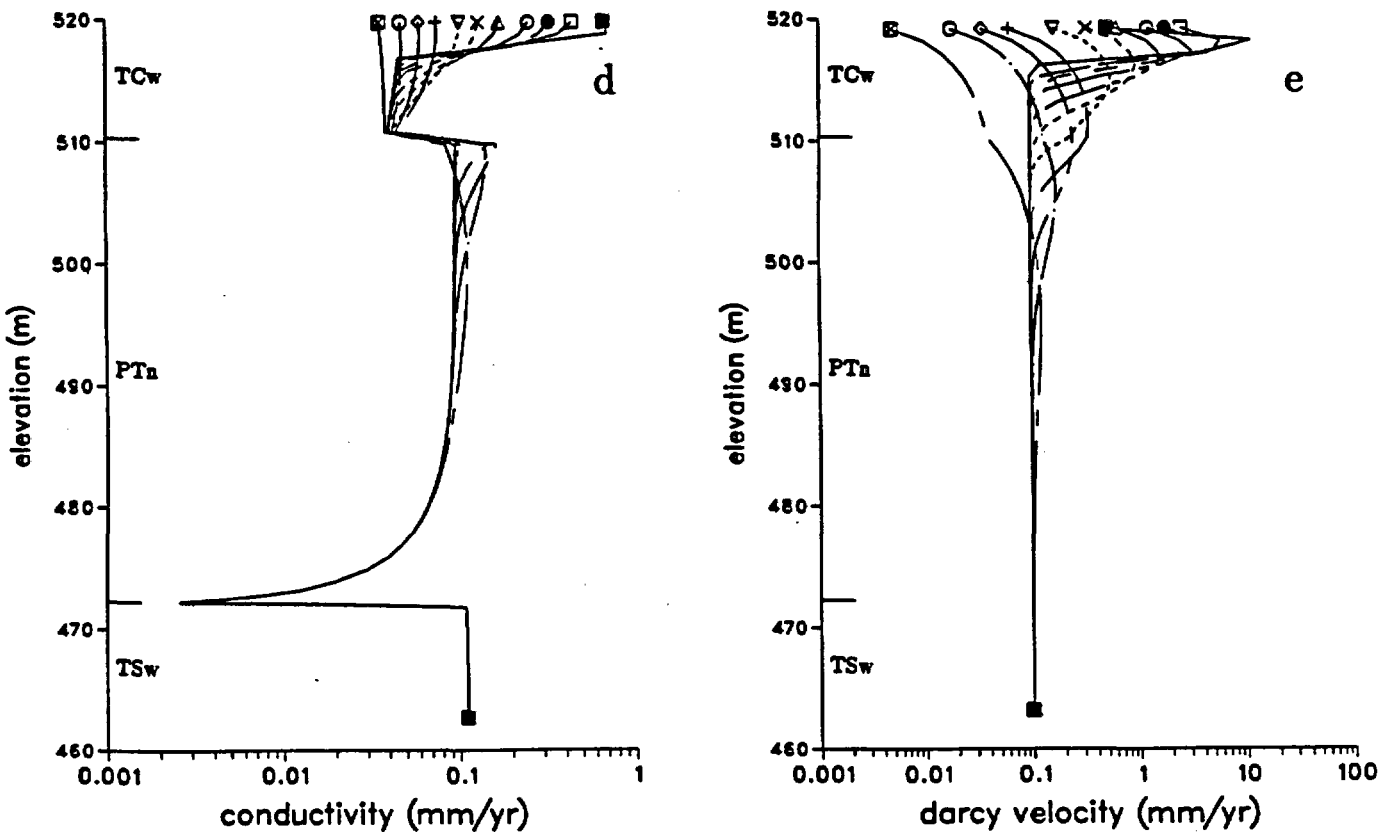

Figure 13. Continued

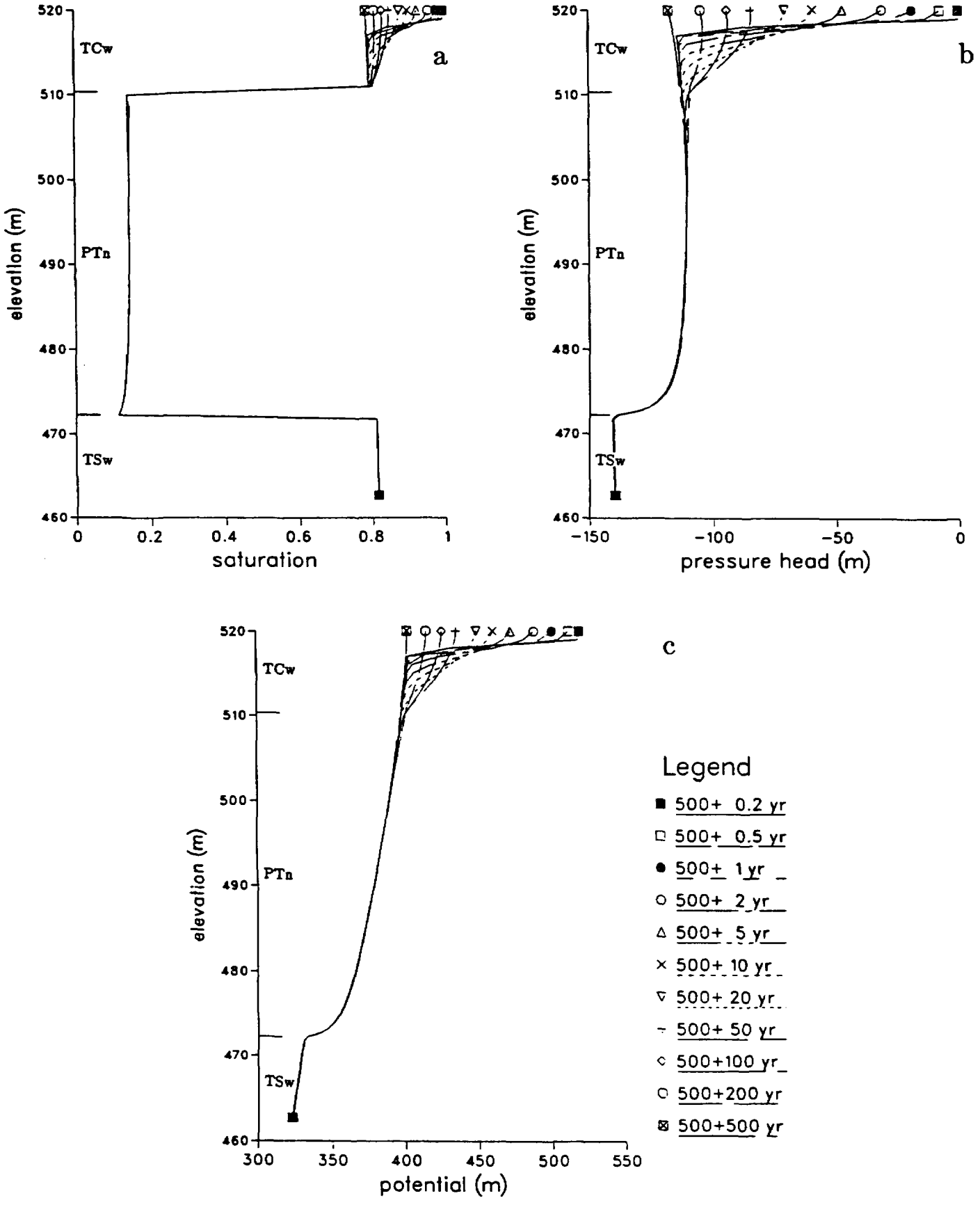

Figure 14. Results for the Second Cycle for 500-yr x 0.1 mm/yr Transient-Pulse Infiltration

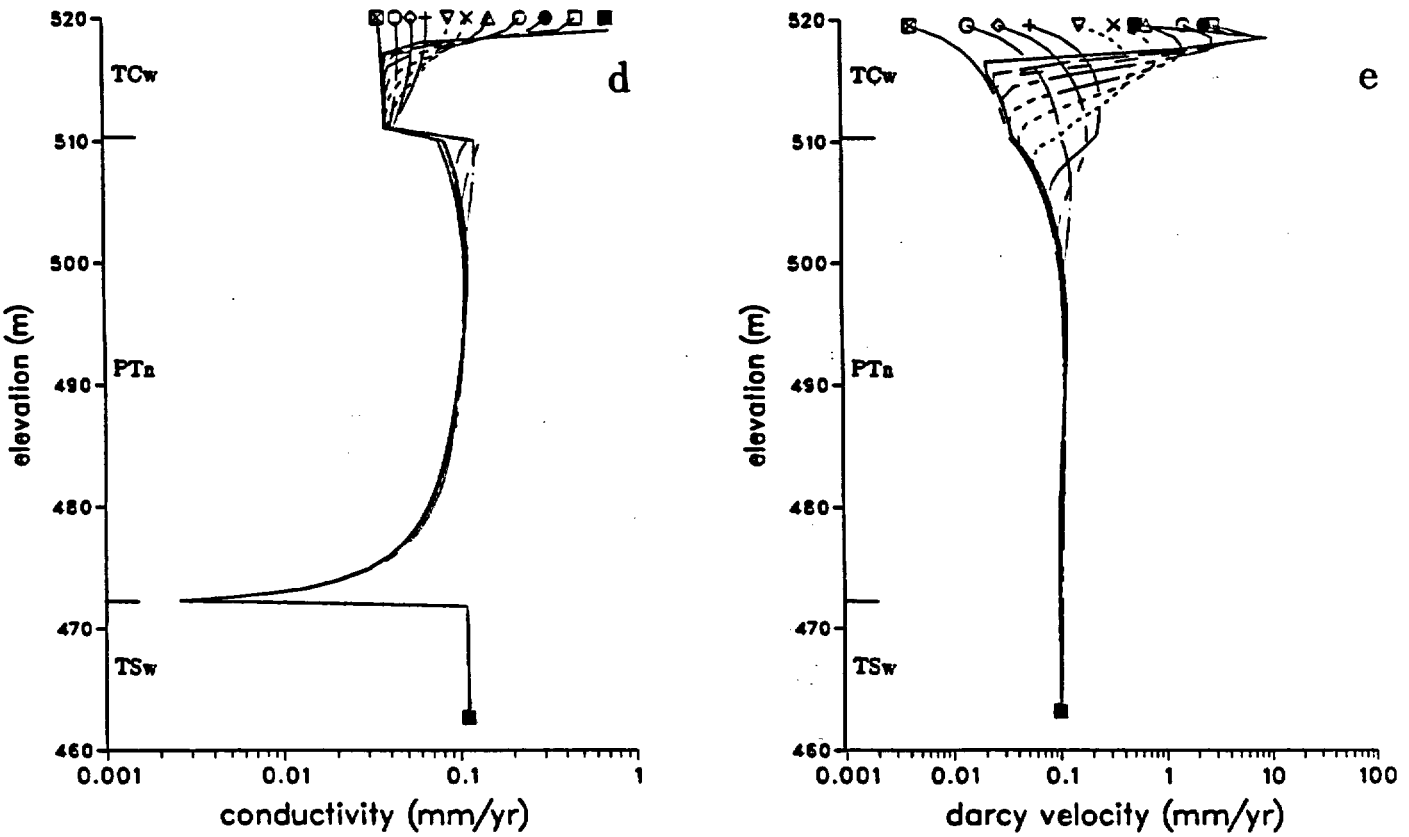

Figure 14. Continued

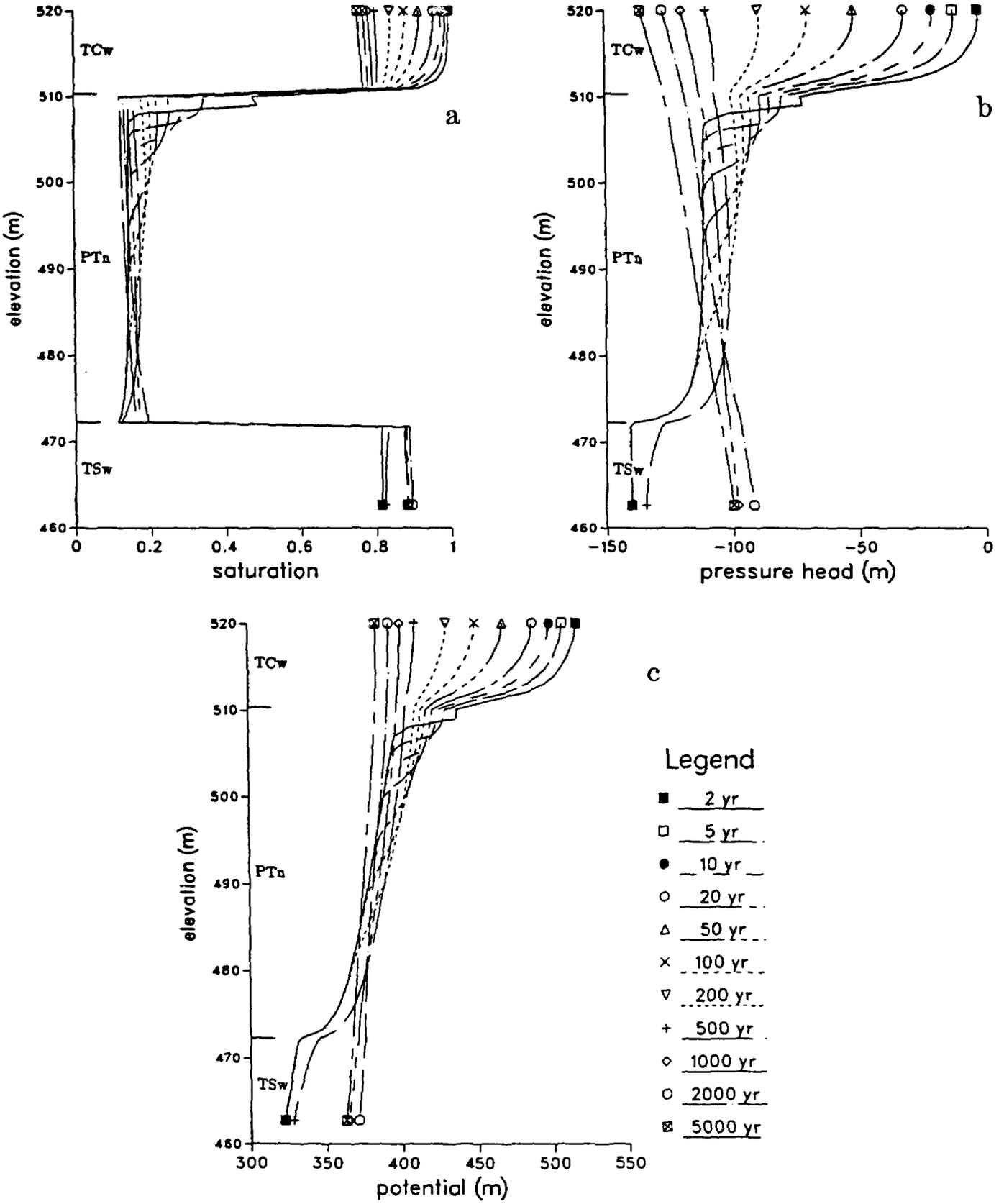

Figure 15. Results for First Cycle of 5,000-yr x 0.1 mm/yr Transient-Pulse Infiltration

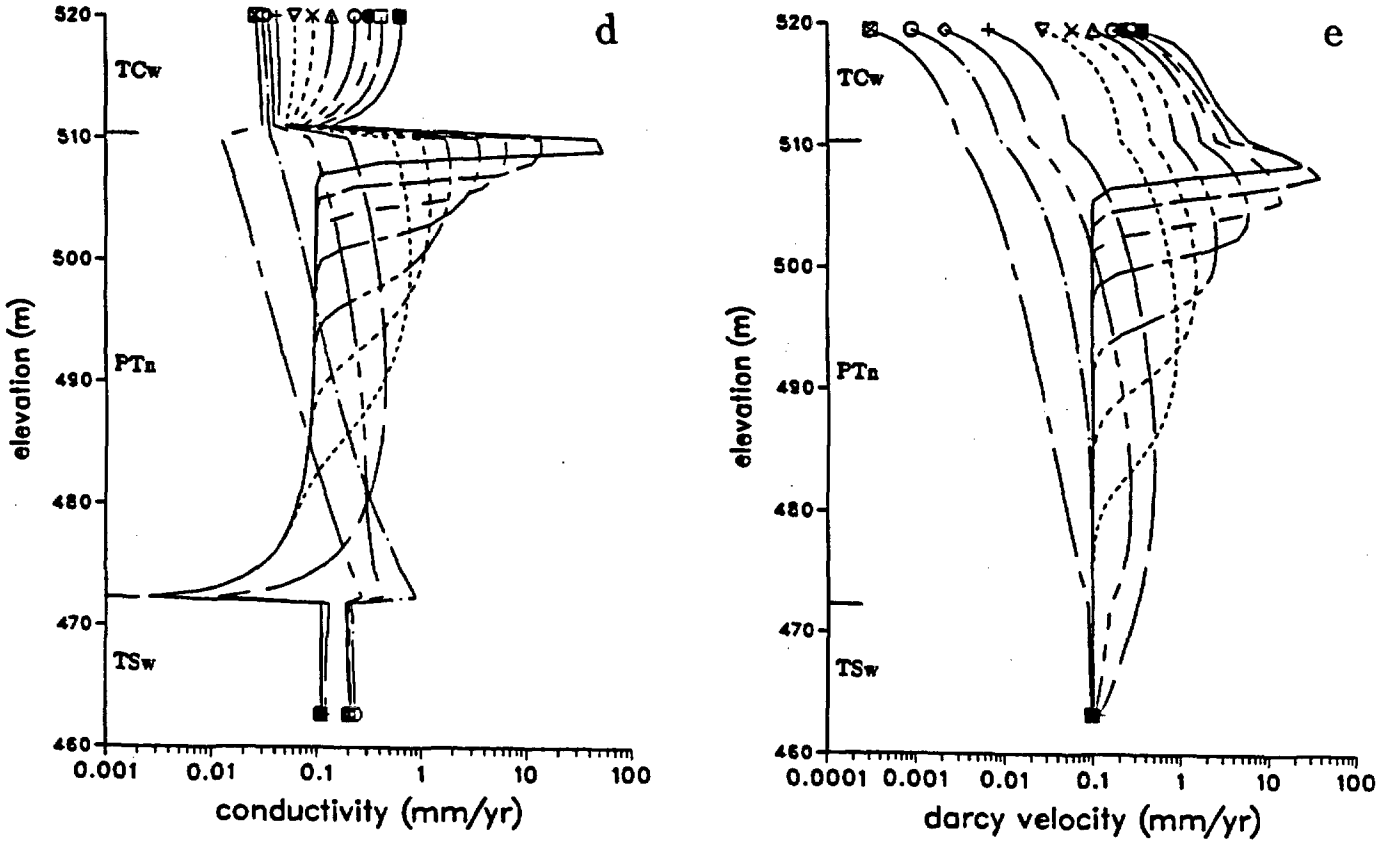

Figure 15. Continued

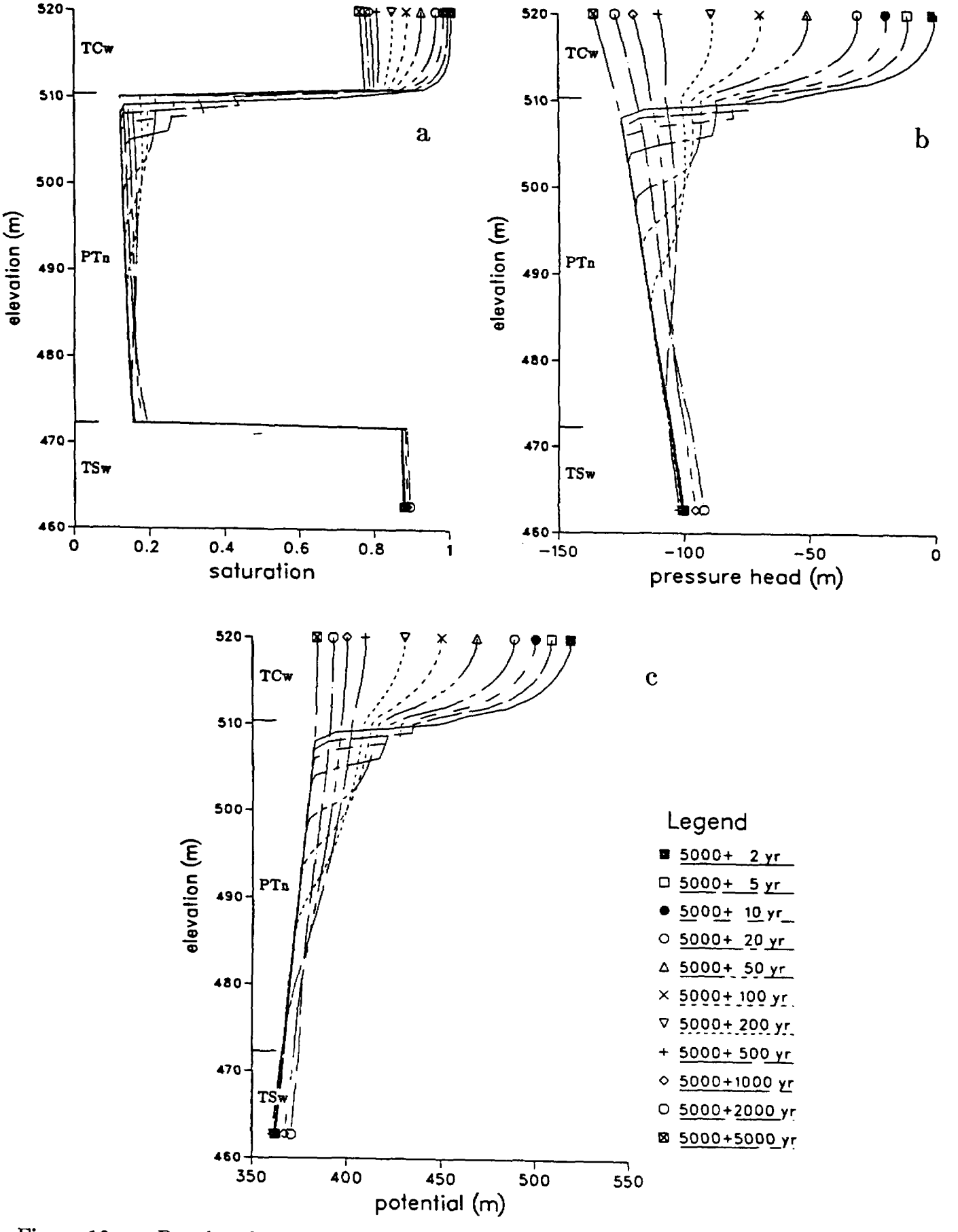

Figure 16. Results for Second Cycle of 5,000-yr x 0.1 mm/yr Transient-Pulse Infiltration

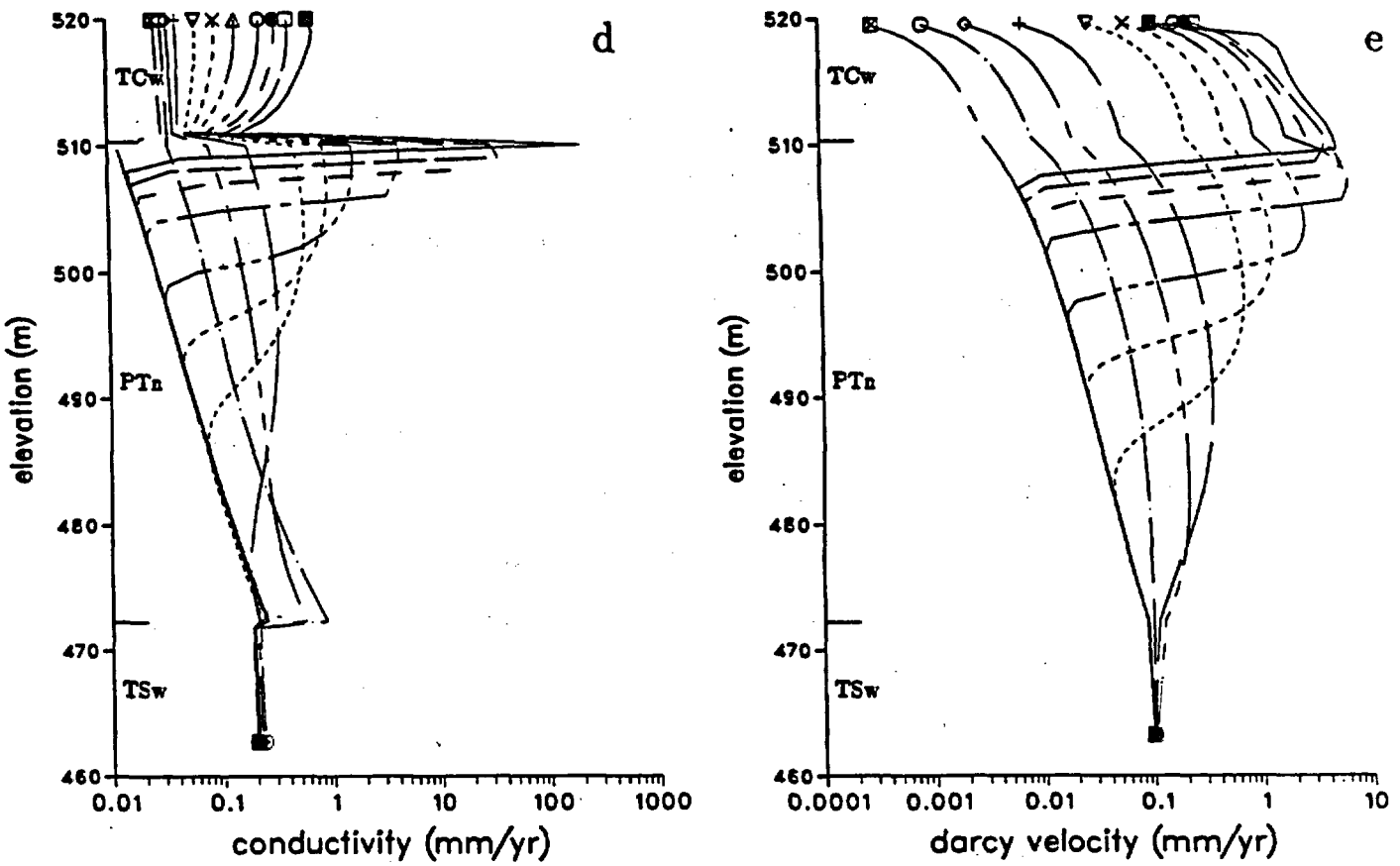

Figure 16. Continued

simulations and the transient-pulse simulations for the 0.1 mm/yr cases. We are mainly interested in the 0.1 mm/yr cases which have steady-state saturation values similiar to the estimated in situ values of 60% to 80% for the welded units. The fixed-gradient approximation breaks down for higher flux cases as we shall discuss after we present the 0.1 mm/yr results.

The infiltration over the whole of Yucca Mountain can either move downward or laterally. The east-west lateral extent of Yucca Mountain varies from several hundred meters to 2,000 m and is much larger than the thickness of the nonwelded units. Since we do not model the lateral variation in saturation and ignore the potential effects of fault zones, we consider a small section in the middle of Yucca Mountain with a single column of width 100 m. Composite medium models are used for the fractured, porous units to estimate the lateral flows.

The effects of lateral leakage in nonwelded units on the steady-state infiltration profiles are shown in Figure 17. Two cases with different assumptions about the isotropy of the permeability are simulated. In the first case, the horizontal permeability of the Paintbrush nonwelded unit is equal to the vertical permeability. For this case, lateral flow removes only a small fraction (approximately 2%) of the total infiltration from the downward flux through the Topopah Spring and other lower units to the water table (Fig. 17e). In the second case, we increase by one-hundred-fold the saturated permeability of a 3.8 m-thick section in the middle of the Paintbrush nonwelded unit (Fig. 17d). With the hydraulic conductivity of the middle one-tenth of this nonwelded unit increased by a factor of 100, we effectively make the horizontal conductivity of the whole nonwelded unit anistropic (Rulon, Bodvarsson, and Montazer, 1985). We also allow the vitric Calico Hills nonwelded unit to have lateral flow. With anisotropic Paintbrush and lateral flows in two nonwelded units, the lateral flow increases approximately ten-fold (Fig. 17e). The saturation, pressure head, and potential

profiles with lateral flows are not significantly different from the profiles with no lateral flow (Figs. 17a, b, and c).

The fixed-gradient approximation can be used to estimate the amount of lateral flow if the flow magnitudes are small. If the lateral-flow magnitudes are large, significant lateral variations of saturation and pressure can occur. For example, if laterally flowing water accumulates toward the east, it will result in decreasing saturations toward the west. The corresponding capillary pressure gradient will act against the eastward component of the gravity gradient and decrease the lateral flow magnitudes. The fixed-gradient approximation does not take this effect into account, although the effects of a saturation gradient could be significant. In the discussion of the differences between 0.1 mm/yr and 0.5 mm/yr vertical steady-state infiltration rates through the Paintbrush nonwelded unit, we noted that the vertical saturation gradient can greatly increase or suppress the vertical gravity gradient. Similiar coupling between lateral saturation and gravity gradients is expected in the lateral direction. The fixed-gradient approximation should be used judiciously. If it is applied indiscriminately, misleading results could be produced. Using the fixed-gradient approximation for the 0.5 mm/yr case, the conductivity in Paintbrush nonwelded unit is so large (Fig. 8d) that the explicitly estimated magnitude of the lateral flow exceeds the infiltration rate. Unrealistic flow reversals occur for the nodes below the Paintbrush nonwelded unit. These unphysical results are caused by overestimation of the lateral flow due solely to the fixed-gradient approximation. Accounting for lateral saturation gradients would more realistically predict the magnitude of lateral flow. Thus, the fixed-gradient approximation breaks down for the high-flux cases. We need to go beyond the single vertical column model to more accurately estimate the effects of lateral flow. To properly model lateral flow in cases with high fluxes, we need to simulate the lateral variations of the saturation

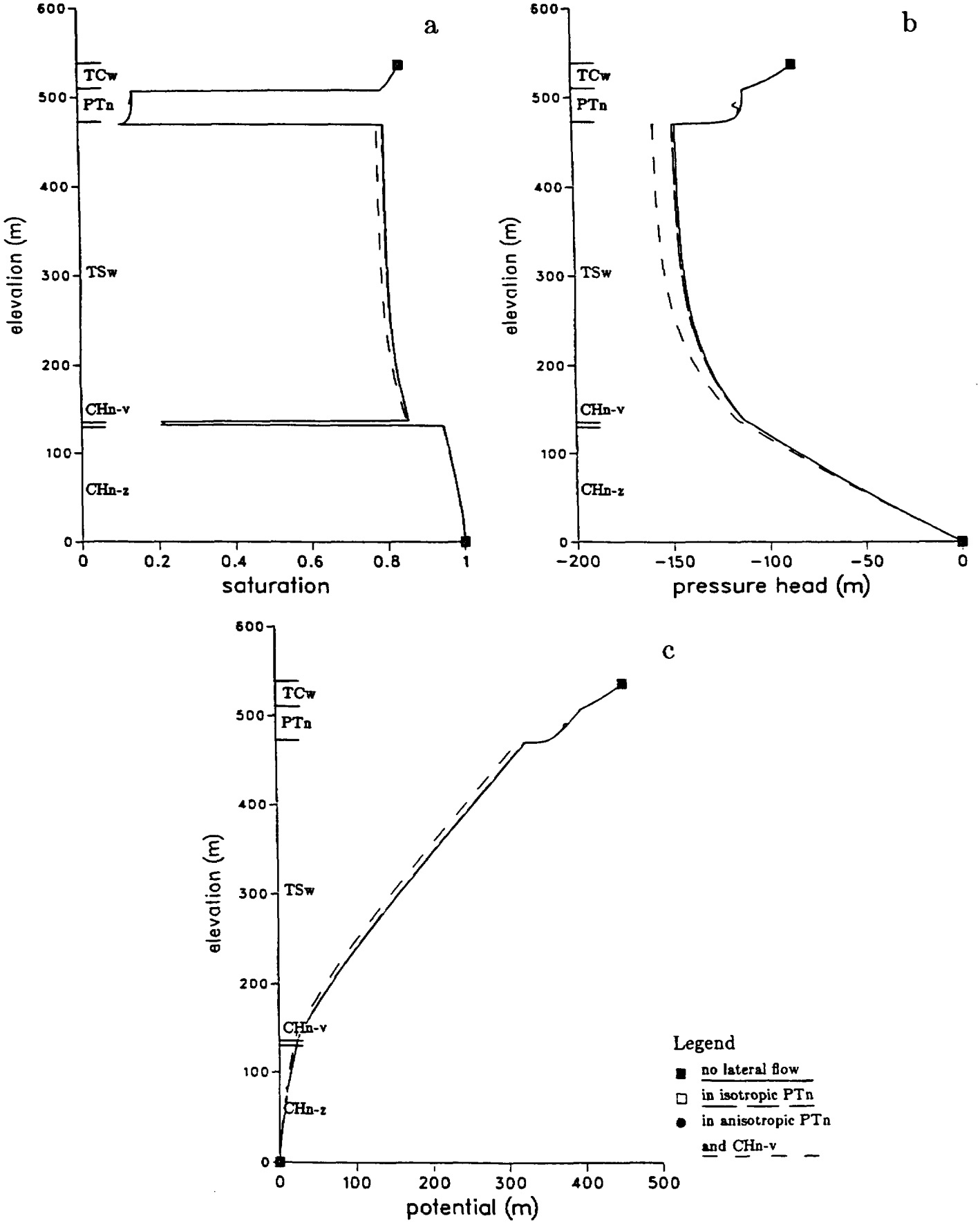

Figure 17. Results for 0.1 mm/ yr Steady-State Infiltration with Lateral Flows

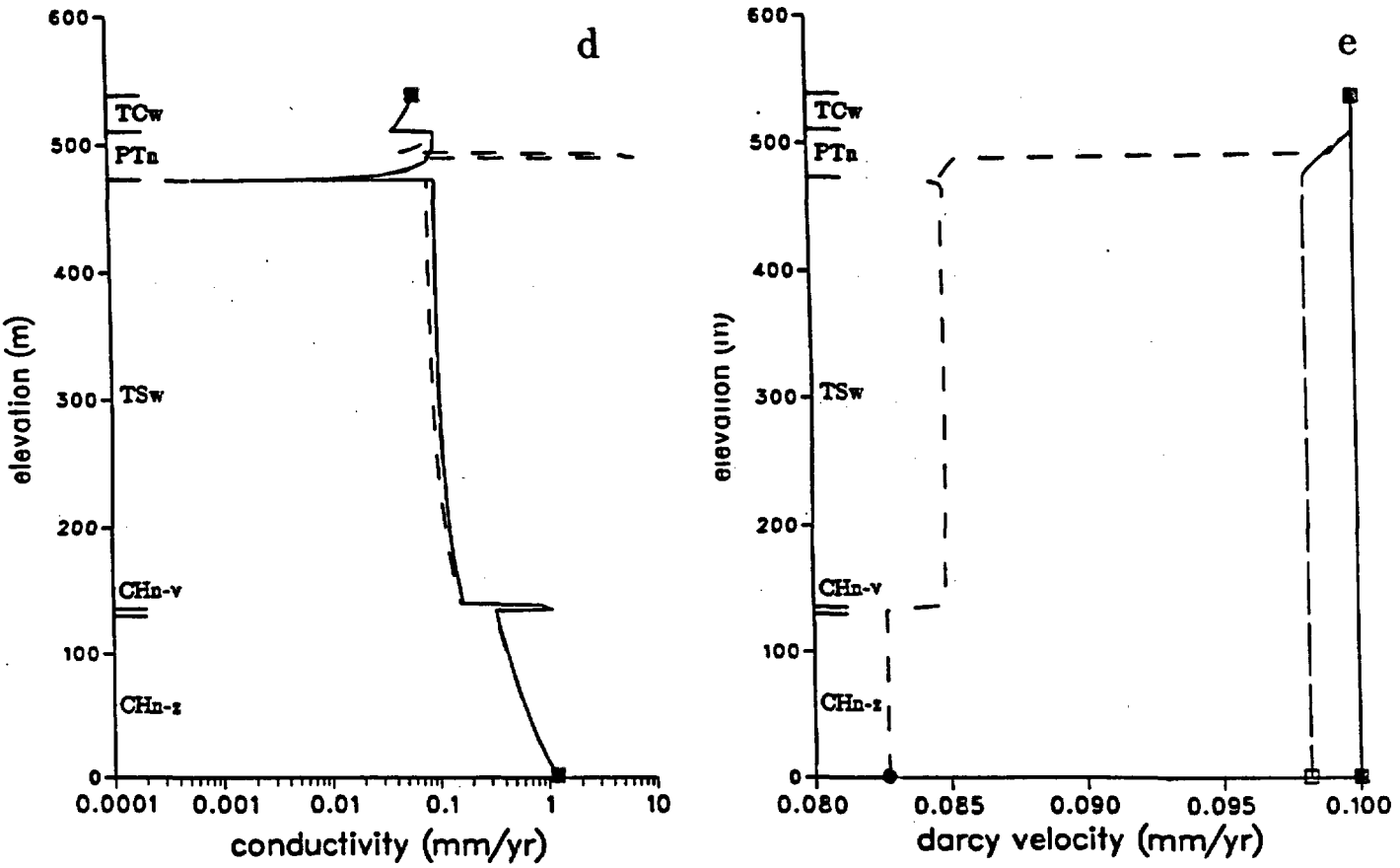

Figure 17. Continued

and pressure fields. The results based on such a cross-section model, with both vertical and lateral variations taken into account, depend on the boundary conditions and material properties of fault zones along the boundaries of the modeled region (Rulon, Bodvarsson, and Montazer, 1985).

6.0 Pulse Infiltration Through Unsaturated Units

In this section, we again simulate pulses of infiltration. However, instead of using a discrete fracture, porous matrix model, as described in the previous section, we use a composite-medium model to represent all welded and nonwelded units from the surface to the water table. Two 5,000-yr pulses are simulated: one corresponding to 0.1 mm/yr average infiltration rate with lateral flow and the other corresponding to 0.5 mm/yr average infiltration rate without lateral flow. For the 0.1 mm/yr case, we investigate whether a large pulse of water prefers moving downward or laterally. For the 0.5 mm/yr case, we are interested in whether the unsaturated system can damp out pulse effects and remain partially saturated for this high flux case with an all-unit model.

For the 5,000-year x 0.1 mm/yr pulse case, an infiltration rate of 2,500 mm/yr is applied for 0.2 yr to the Tiva Canyon welded unit below the fully saturated interval which has all its available pore space occupied by infiltrated water. The total amount of water applied to the system in 0.2 yr corresponds to all the infiltration in 5,000 yr. The Paintbrush nonwelded unit is anisotropic with an one-hundred-fold high-permeability layer in the middle one-tenth of this unit. The fixed-gradient approximation is used to estimate lateral flows in the Paintbrush nonwelded unit and the vitric Calico Hills unit. The initial conditions correspond to the profiles of 0.1 mm/yr steady-state infiltration (Fig. 17). The results of the transient profiles of saturation, pressure head, potential, conductivity, and Darcy velocity for the first 5,000 yr are shown in Figure 18. Similiar

results are obtained for additional cycles of pulse infiltration as shown in Figure 19 for the third cycle (10,000 yr to 15,000 yr). The damping of the pulse and the penetration of the transient effects for this composite-medium, all-unit simulation agrees with the earlier discrete-fracture, upper-unit results with finer meshes shown in Figures 15 and 16. The effects of the pulsing reach the top of Topopah Spring welded unit in 1,000 yr and penetrate the upper part of the Topopah Spring welded unit.

Most of the damping of the pulse occurs in the Paintbrush nonwelded unit. A large 5,000-yr pulse can saturate the matrix, initiate fracture flow, and generate complex flow field in the Tiva Canyon welded unit. When the transient effects move into the Paintbrush nonwelded unit, its large pore volume and highly nonlinear unsaturated characteristics can effectively accommodate and absorb the highly transient and intense water pulses. Only mild perturbations reach the Topopah Spring welded unit.

Figure 20 illustrates the propagation and damping of the pulse in the Paintbrush nonwelded unit. It also compares the change of the lateral flow versus the change in downward infiltration flow. The large mass flux passing through the top Tiva Canyon-Paintbrush interface at 100 yr is damped out as it moves down the Paintbrush nonwelded unit. Some of the water moves out of the column laterally. The total lateral mass flux increases slightly at 1,000 yr. With this increase, the mass flux passing the lower Paintbrush-Topopah Spring interface decreases slightly. However, at later times around 2,000 yr, the mass flux at the lower interface increases by a larger amount than the increase in the total lateral flow. As the pulse of water passes through the Paintbrush nonwelded unit, it increases the saturation and conductivity locally node by node. The increases in conductivity values will, in turn, enhance the lateral flow magnitudes in the fixed-gradient approximation. However, the competing process of moving

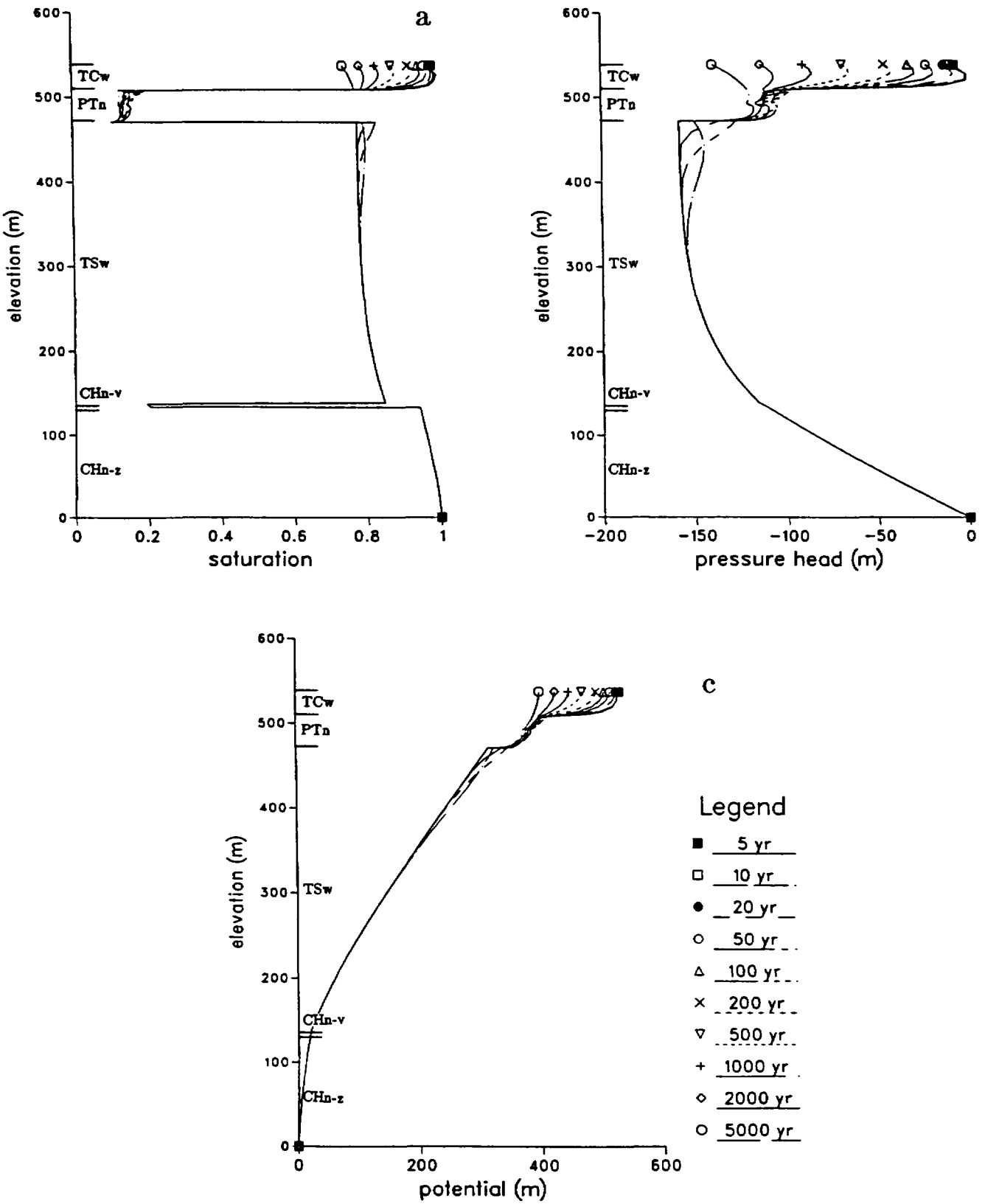

Figure 18. Results for First Cycle of 5,000-yr x 0.1 mm/yr Transient-Pulse Infiltration with Lateral Flows

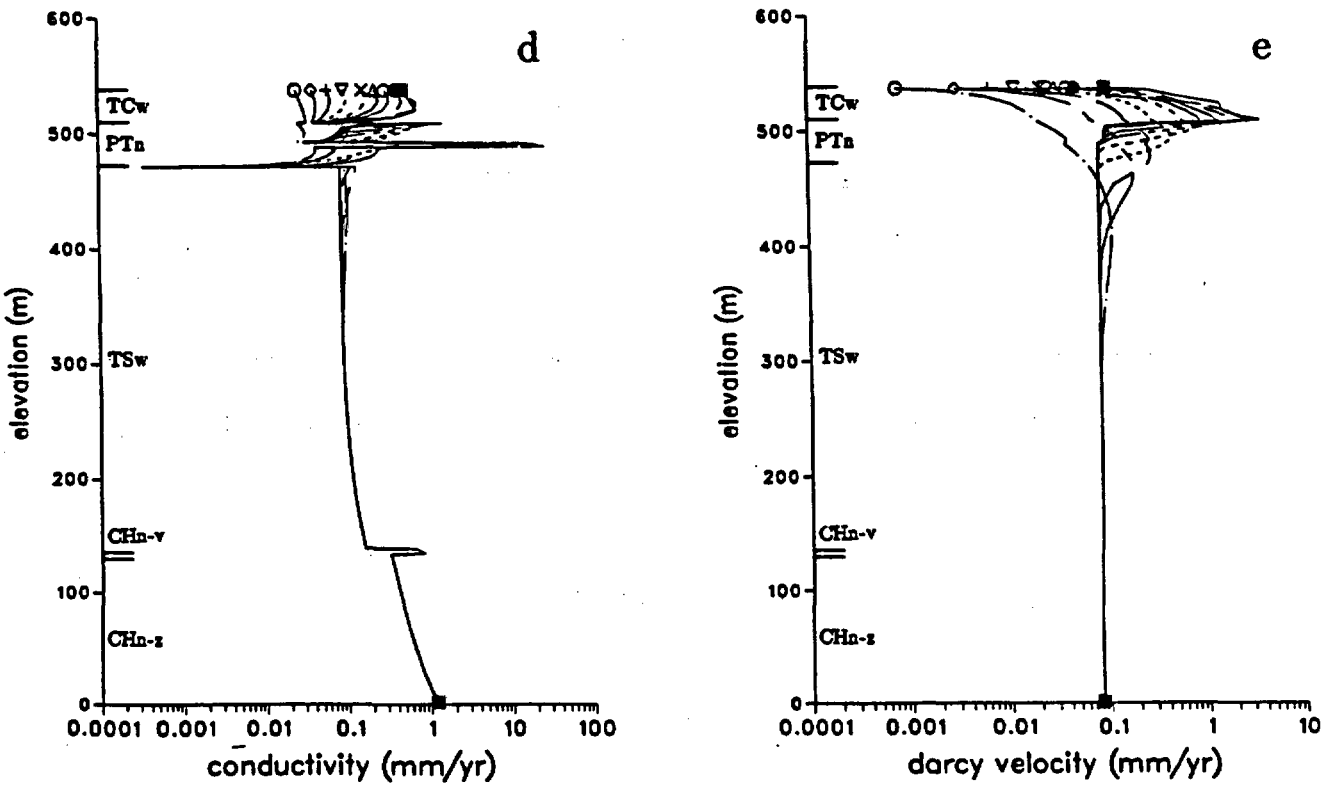

Figure 18. Continued

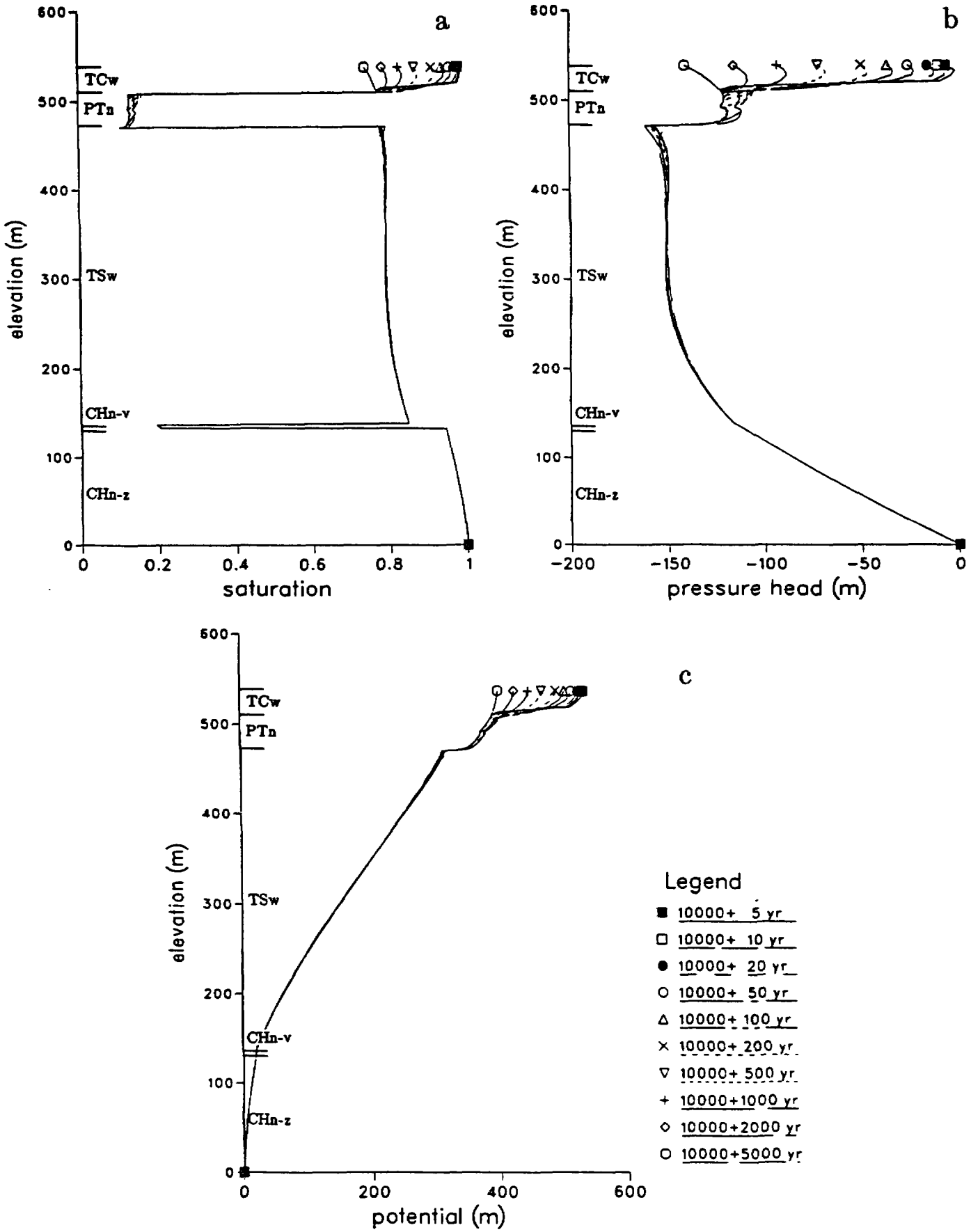

Figure 19. Results for Third Cycle of 5,000-yr x 0.1 mm/yr Transient-Pulse Infiltration with Lateral Flows

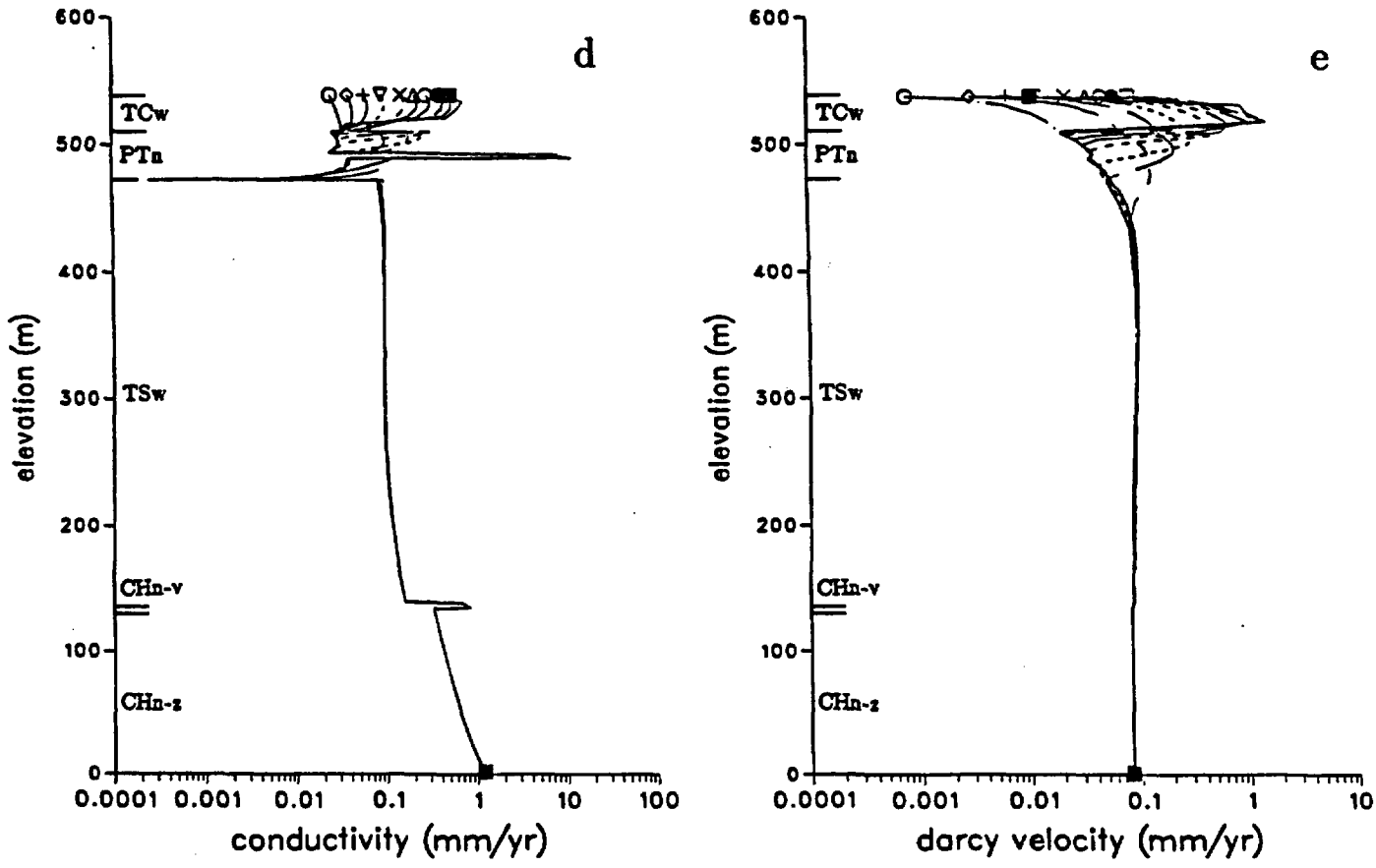

Figure 19. Continued

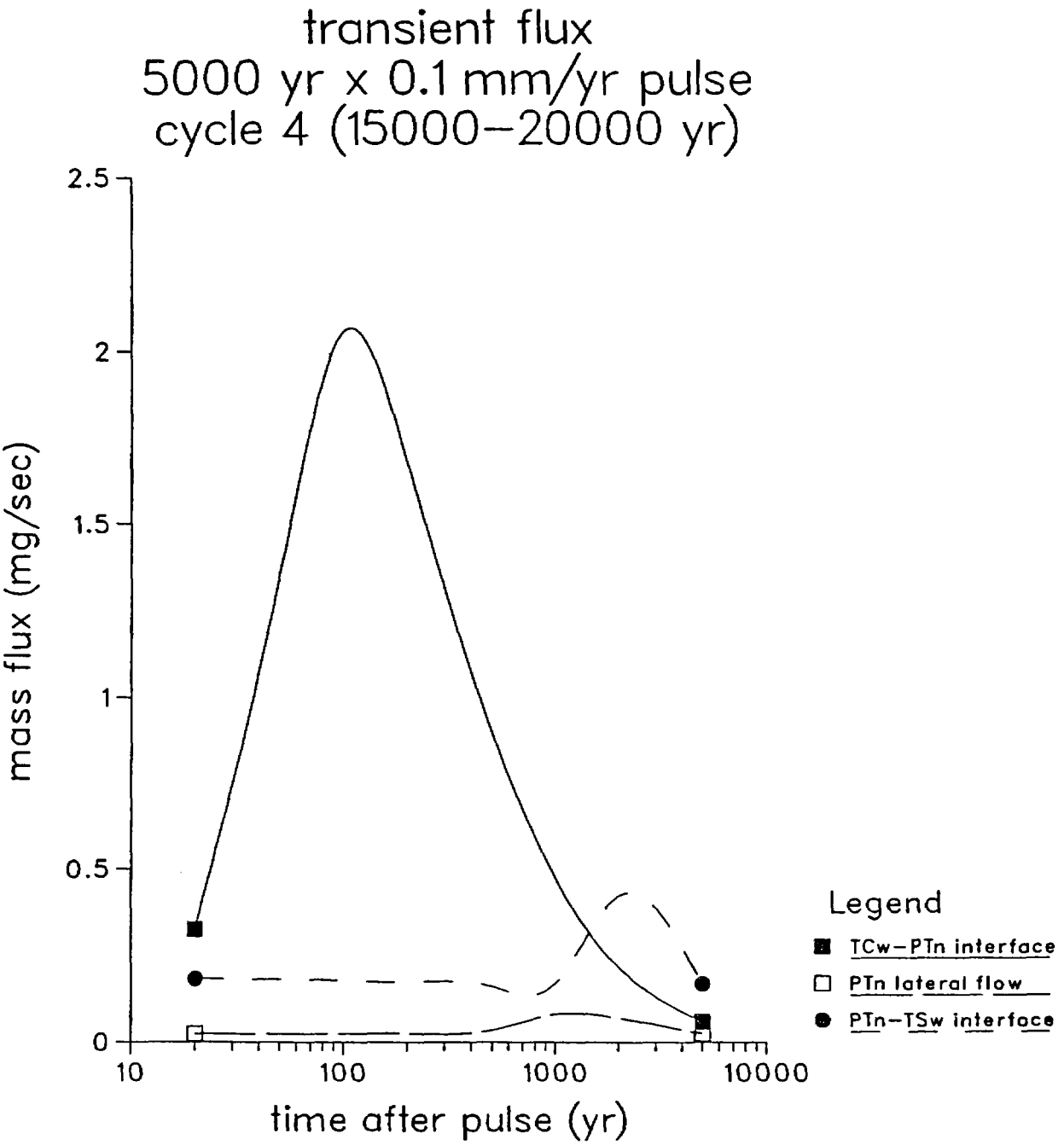

Figure 20. Propagation and Damping of 5,000-yr x 0.1 mm/yr Pulse with Lateral Flow

downward can also benefit from the local saturation increases. The local saturation increases will enhance the saturation gradient. The saturation gradient, together with the gravity gradient, drive the water downward into the Topopah Spring welded unit.

The highest pulse we apply to the Yucca Mountain column model is a 5,000-yr x 0.5 mm/yr pulse case. The infiltration pulse rate within 0.2 yr is 12,500 mm/yr and the initial condition before the first cycle corresponds to 0.5 mm/yr steady-state infiltration (Fig. 8). For this high flux case, we do not use the fixed-gradient approximation, which overestimates the lateral flow and yields unphysical results in the steady-state simulations discussed earlier. The high infiltration rate of 12,500 mm/yr can saturate the Tiva Canyon welded unit within 0.2 yr. The transient changes in saturation, pressure head, potential, conductivity, and Darcy velocity after the first and the second pulse are shown in Figures 21 and 22. For this high-pulse, high-flux case, the Topopah Spring welded unit remains partially saturated (Figs. 21a and 22a). The Paintbrush nonwelded unit damps and absorbs the pulses. We may require even higher pulses and higher fluxes to initiate fracture flow in the Topopah Spring unit.

7.0 Summary and Discussion

Table 5 summarizes the steady-state and transient-pulse infiltration calculations discussed in this report. All the simulations use one set of representative matrix and fracture properties for the welded and nonwelded units (Tables 1 and 2). For this particular set of parameters of the alternating layer system, the net infiltration rate through the Topopah Spring welded unit is likely to be 0.1 mm/yr. With 0.1 mm/yr infiltration, the simulated saturation value in the Topopah Spring welded unit is close to the in situ value of 60% to 80% in the matrix. We focus more on the 0.1 mm/yr cases for this reason.

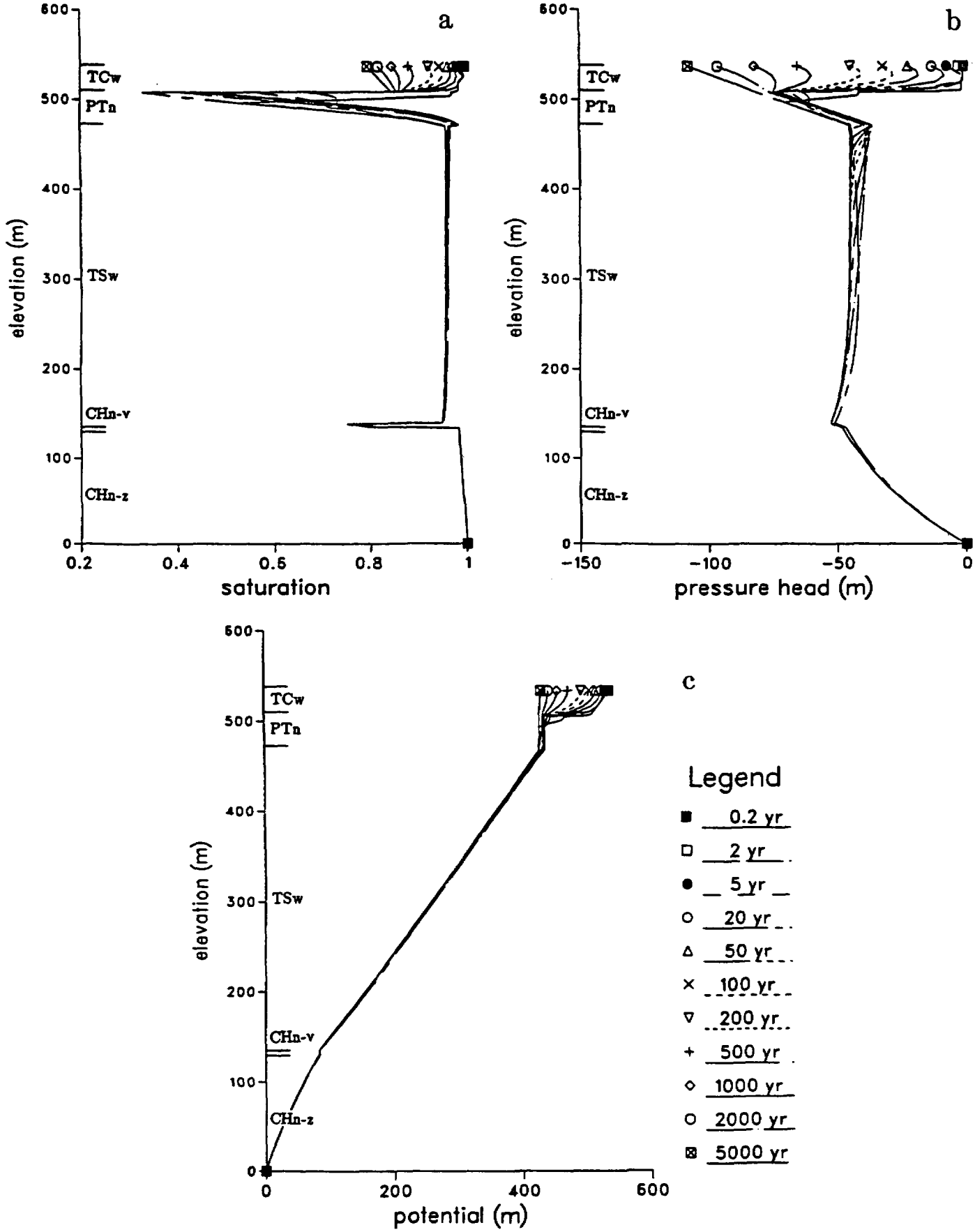

Figure 21. Results for First Cycle of 5,000-yr x 0.5 mm/yr Transient-Pulse Infiltration

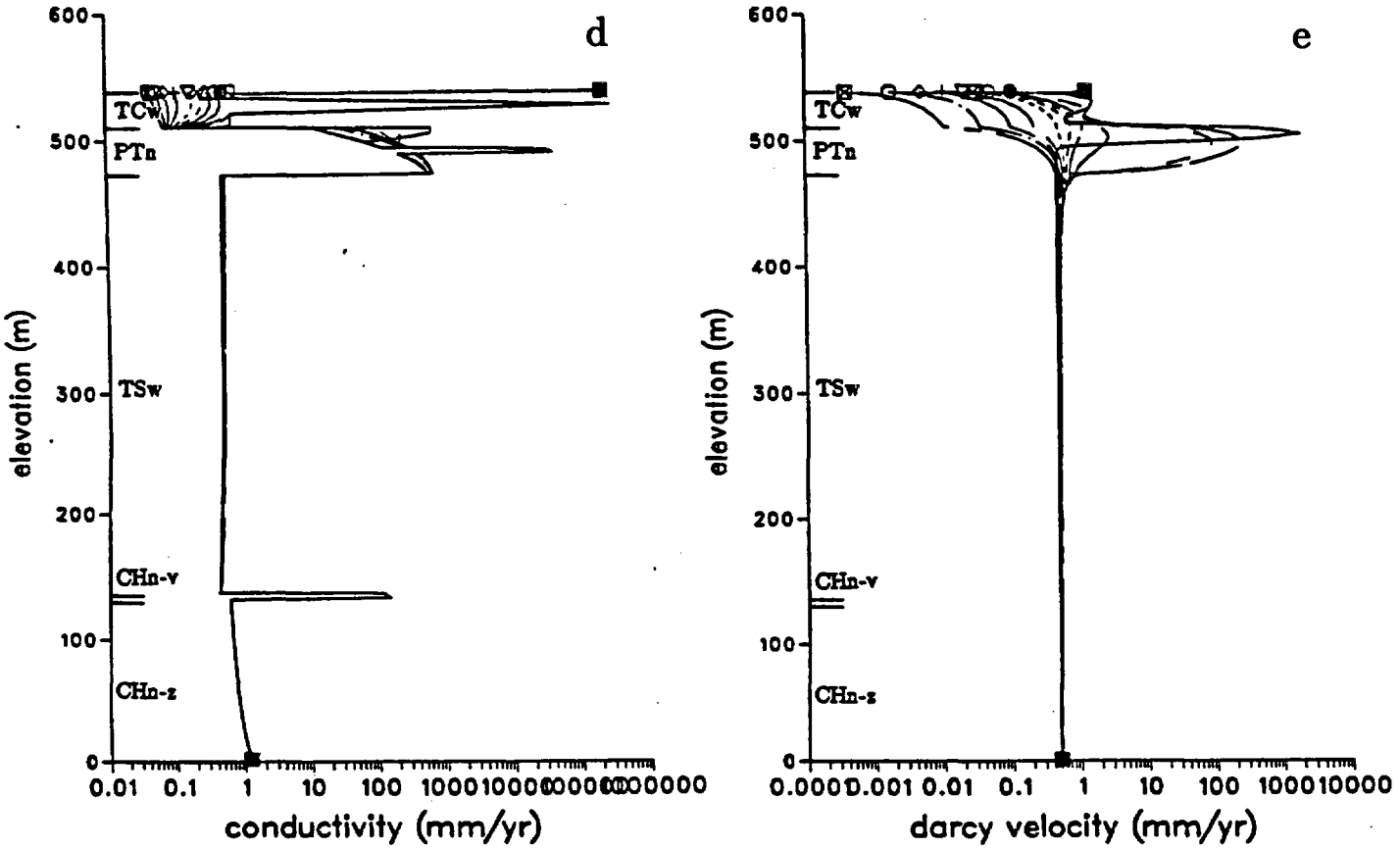

Figure 21. Continued

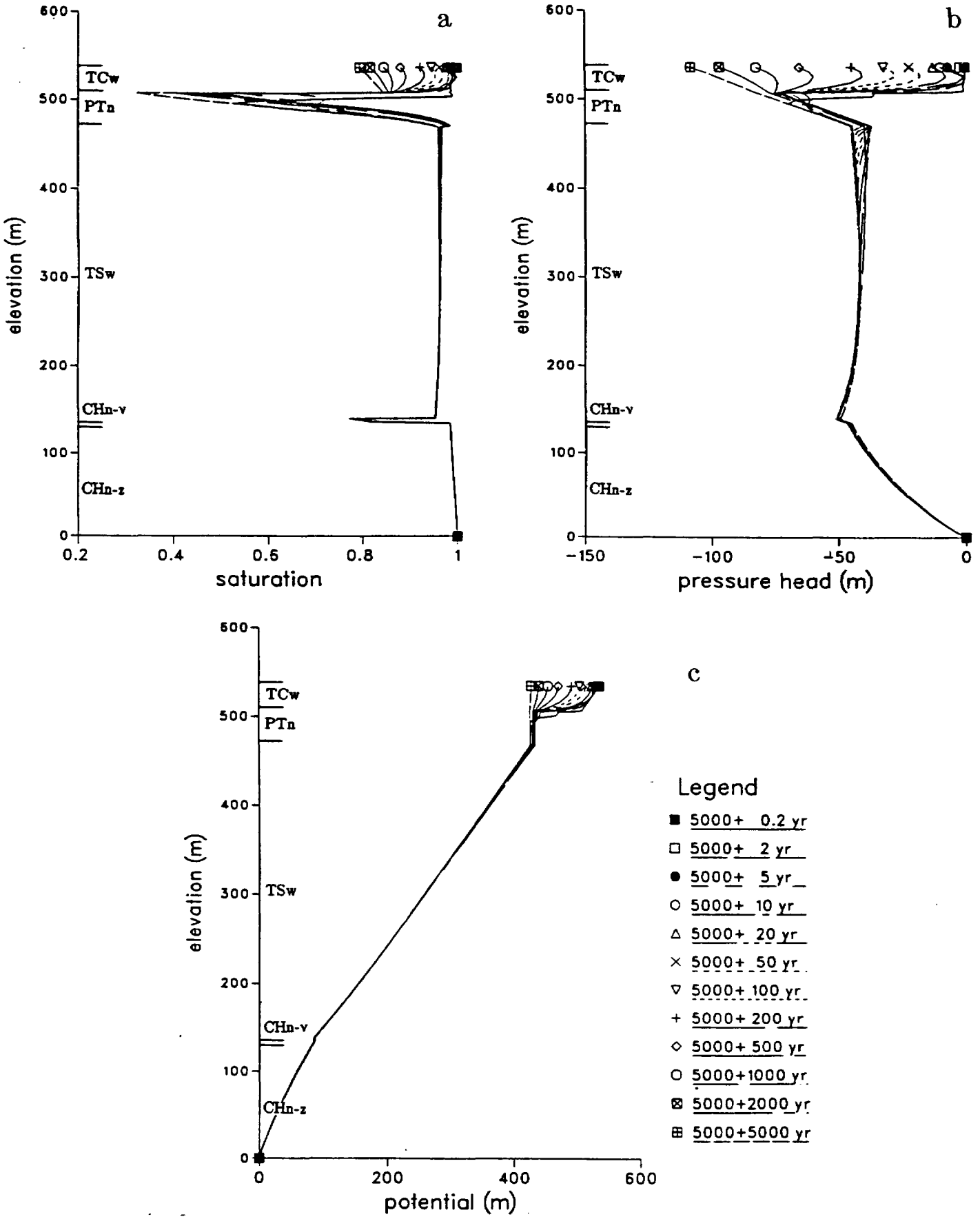

Figure 22. Results for Second Cycle of 5,000-yr x 0.5 mm/yr Transient-Pulse Infiltration

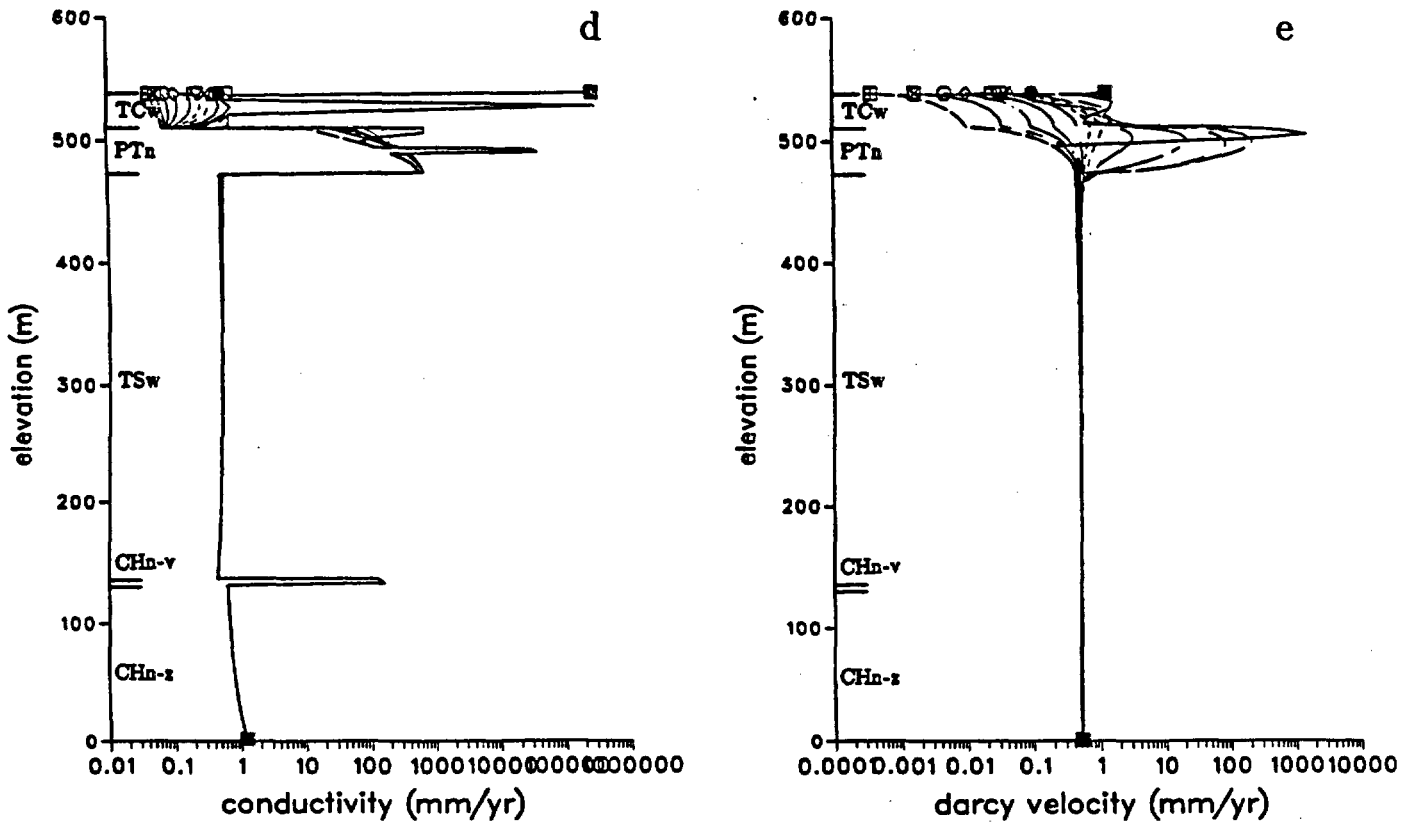

Figure 22. Continued

The steady-state infiltration calculations are first carried out to define the initial conditions for the pulse infiltration calculations. The thick Topopah Spring welded unit has a relatively uniform saturation profile with the partially saturated hydraulic conductivity equal to the net infiltration rate. Both the steady-state and the transient-pulse simulation results are sensitive to mesh designs and solution controls. For the 0.1 mm/yr cases, we need to have a very fine mesh, started with 0.01 m grading, above the Topopah-Paintbrush interface to properly model the sharp changes in pressure and saturation across the interface. For discrete fracture, porous matrix model with discrete fracture nodes and nested porous matrix nodes, the discretization of the matrix block also needs fine grading near the matrix-fracture interfaces. A 10-continuum nested mesh for the matrix blocks generally takes fewer iterations to reach a solution than a 5-continuum mesh. In some cases if we use more coarse mesh, we will get artificial ponding in some nodes. However for the 0.5 mm/yr case, the permeability in the Paintbrush is high, and we do not need such a fine mesh to generate good results.

Table 5. Steady-State and Transient-Pulse Infiltration Simulations

Cases	Main Features
0.1 mm/yr steady-state	3% CHn-v, 97% CHn-z
0.1 mm/yr steady-state	100% CHn-v
0.5 mm/yr steady-state	anistropic PTn
1-yr x 0.1mm/yr pulse	0.5 mm/yr for 0.2 yr
5-yr x 0.1 mm/yr pulse	2.5 mm/yr for 0.2 yr
50-yr x 0.1 mm/yr pulse	25 mm/yr for 0.2 yr
500-yr x 0.1 mm/yr pulse	250 mm/yr for 0.2 yr
5,000-yr x 0.1 mm/yr pulse	2,500 mm/yr for 0.2 yr
0.1 mm/yr steady-state	lateral flow in isotropic PTn
0.1 mm/yr steady-state	lateral flows in anisotropic PTn and CHn-v
5,000-yr x 0.1 mm/yr pulse	2,500 mm/yr for 0.2 yr with lateral flows
5,000-yr x 0.5 mm/yr pulse	12,500 mm/yr for 0.2 yr without lateral flows

We use the discrete-fracture, porous-matrix model for the welded units in the transient simulations for cycles of pulse infiltration through the Tiva Canyon welded unit, the Paintbrush nonwelded unit, and the Topopah Spring welded unit. The pulses with different rates corresponding to different periods are applied to the fractures at the top of the Tiva Canyon welded unit. The results show that the water initially does not accumulate in the fractures, and water moves quickly into the matrix block. The water distributes nearly evenly in the matrix block. Only when the top matrix block approaches full saturation, will substantial changes occur in the next block below. The fast-suction, even-wetting behavior allows us to adopt a simple sharp-wetting-front approximation to simulate the long-term changes induced by the pulses. For the units remaining partially saturated with infiltration flux less than the matrix saturated conductivity, we can use a composite-medium model to represent both the discrete fractures and the porous matrix.

For average infiltration rates of 0.1 to 0.5 mm/yr and pulse periods up to 5,000 yr, the transition from partially saturated conditions to fully saturated conditions and the onset of fracture flows occur only in the Tiva Canyon welded unit when the total amount of infiltration water within a period is applied to the column within 0.2 yr. As the water moves down into the Paintbrush nonwelded unit, the large pore and nonlinear unsaturated characteristics of this unit can effectively damp out the transient infiltration pulses during the first few thousand years. The Topopah Spring welded unit remains partially saturated with small changes in saturation, pressure head, and potential from the steady-state values.

The column models used in the steady-state and pulse infiltration simulations in this report do not take into account the lateral variations in the flow field and the effects of the fault zones on the boundaries. We use a fixed-gradient approximation to estimate the lateral flows in the Paintbrush nonwelded unit and

the vitric Calico Hills unit. The fixed-gradient approximation estimates the lateral flows by the tilting angle of the bedding planes, together with the partially saturated conductivities and the vertical thicknesses of the nodes in the nonwelded units. This approximation is applicable if the estimated lateral flows are smaller than the vertical flows so that there will be no substantial redistribution of saturation in the lateral direction. For the cases with steady-state 0.1 mm/yr, the lateral flows estimated by the fixed-gradient approximation are indeed small, even when we replace the isotropic Paintbrush unit with an anisotropic unit that has a high permeability layer in the middle. In the corresponding transient-pulse cases, the pulses prefer to move downward with a small fraction of water removed laterally out of the main downward infiltration paths. For higher fluxes, wider regional cross-sectional models are needed to simulate both the vertical and lateral variations in the flow field to determine the lateral flows of this fractured, porous alternating layer system.

Further studies are also needed to address the effects of film flows along fracture surfaces, reduced permeability skin at the surfaces of matrix blocks to retard fracture-to-matrix flows, hysteresis, entraped air pockets in rough-walled fractures and porous matrix blocks, and other noncapillary mechanisms that may promote fracture flows and reduce capillary force sucking water into the matrix. The strong suction is responsible for the matrix-dominant flow behavior in the partially saturated, fractured porous medium. If the onset of fracture flows could be demonstrated to be unlikely under ambient conditions and under extreme flooding events, a partially saturated, fractured formation could be a good candidate for waste isolation.

8.0 References

Barr, G. E., Reduction of the Well Test Data for Test Well USW H-1, Adjacent to the Neveda Test Site, Nye County, Neveda, SAND84-0637, Sandia National Laboratories, Albuquerque, NM, 41 p, 1985.

Beven, K. and P. Germann, Macropores and Water Flow in Soils, *Water Resour. Res.*, 18(5), pp. 1311-1325, 1982.

Carslaw, H. S. and J. C. Jaeger, *Conduction of Heat in Solids,* Oxford University Press, 510 p, 1959.

Davidson, M. R., Numerical Calculation of Saturated-Unsaturated Infiltration in a Cracked Soil, *Water Resour. Res.*, 21(5), pp. 709-714, 1985.

DOE (U. S. Department of Energy), Nuclear Waste Policy Act Environment Assessment of the Neveda Nuclear Waste Storage Investigations (NNWSI) Project, May 1986.

Edwards, W. M., R. R. van der Ploeg, and W. Ehlers, A Numerical Study of the Effects of Noncapillary-Sized Pores upon Infiltration, *Soil Sci. Soc., Am. J.*, 43, pp. 851-856, 1979.

Hoogmoed, W. B. and J. Bouma, A Simulation Model for Predicting Infiltration into Cracked Clay Soil, *Soil Sci. Soc. Am. J.*, 44, pp. 458-461, 1980.

Klavetter, E. A. and R. R. Peters, Fluid Flow in a Fractured Rock Mass, SAND85-0855c, Sandia National Laboratories, Albuquerque, NM, 48 p, 1985.

Montazer, P., E. P. Weeks, F. Thamir, S. N. Yard, and P. B. Hofrichter, Monitoring the Vadose Zone in Fractured Tuff, Yucca Mountain, Neveda, Proceedings, National Water Well Association Conference on Characterization and Monitoring of the Vadose (Unsaturated) Zone, Denver, CO, November 19-21, 1985.

Montazer, P. and W. E. Wilson, Conceptual Hydrologic Model of Flow in the Unsaturated Zone, Yucca Mountain, Nevada, *Water-Resources Investigations Report 84-4345,* U.S. Geological Survey, Lakewood, CO, 55 p, 1984.

Narasimhan, T. N., M. Alavi, and T. Tokunaga, COVE2A Benchmarking Studies, Memorandum to W. Prindle and N. Hayden, Lawrence Berkeley Laboratory, Berkeley, CA, 1985.

Narasimhan, T. N. and P. A. Witherspoon, Numerical Model for Saturated-Unsaturated Flow in Deformable Porous Media, 1. Theory, *Water Resour. Res.*, 13, pp. 657-664, 1977.

Narasimhan, T. N., P. A. Witherspoon, and A. L. Edwards, Numerical Model for Saturated-Unsaturated Flow in Deformable Porous Media, Part 2, the Algorithm, *Water Resour. Res.*, 14, pp. 255-261, 1978.

Nimick, F. B., S. J. Bauer, and J. R. Tillerson, Recommended Matrix and Rock-

Matrix Bulk, Mechanical and Thermal Properties for Thermomechanical Stratigraphy of Yucca Mountain, Keystone document 6310-85-1, Sandia National Laboratories, Albuquerque, NM, 1984.

Ortiz, T. S., R. L. Williams, F. B. Nimick, B. C. Whittet, and D. L. South, A Three-Dimensional Model of Reference Thermal-Mechanical and Hydrological Stratigraphy at Yucca Mountain, Southern Nevada, SAND84-1076, Sandia National Laboratories, Albuquerque, NM, 1984.

Peters, R. R., Revised Matrix Hydrologic Property Data for Samples Taken from Drill Holes USW G-3 and USW G-4, memorandum to distribution, Sandia National Laboratories, Albuquerque, NM, 10 p, 1984.

Peters, R. R., J. H. Gauthier, and A. L. Dudley, The Effect of Percolation Rate on Water Travel Time in Deep, Partially Saturated Zones, SAND85-0854c, Sandia National Laboratories, Albuquerque, NM, 36 p, 1985.

Peters, R. R., E. A. Klavetter, I. J. Hall, S. C. Blair, P. R. Heller, and G. W. Gee, Fracture and Matrix Hydrologic Characteristics of Tuffaceous Materials from Yucca Mountain, Nye County, Nevada, SAND84-1471, Sandia National Laboratories, Albuquerque, NM, 188 p, 1984.

Pruess, K. and T. N. Narasimhan, A Practical Method for Modeling Fluid and Heat Flow in Fractured Porous Media, *Society of Petroleum Engineering Journal,* pp. 14-26, February, 1985.

Pruess, K., Y. W. Tsang, and J. S. Y. Wang, Modeling of Strongly Heat-derived Flow in Partially Saturated Fractured Porous Media, Proceedings, Hydrogeology of Rocks of Low Permeability, International Association of Hydrogeologists, Memoires, Vol. XVII, pp. 486-487, 1984.

Rubin, J. and R. Steinhardt, Soil-Water Relations During Rain Infiltration, I. Theory, *Soil Sci. Soc. Amer. Proc.* 27, pp. 246-251, 1963.

Rulon, J., G. S. Bodvarsson, and P. Montazer, Numerical Simulations of Flow in the Unsaturated Zone, Yucca Mountain, Nevada, Draft, Lawrence Berkeley Laboratory, Berkeley, CA, 110 p, 1985.

Rush, F. E., W. Thordarson, and D. G. Tyles, Geohydrology of Test Well USW H-1, Yucca Mountain, Nye County, Neveda, USGS-WRI-84-4032, Water Resources Investigations, U. S. Geological Survey, Denver, CO, 1985.

Scott, R. B. and J. Bonk, Preliminary Geologic Map of Yucca Mountain with Geologic Sections, Nye County, Nevada, Open-file Report 84-494, U.S. Geological Survey, Denver, CO, 1984.

Scott, R. B., R. W. Spengler, S. Diehl, A. R. Lappin, and M. P. Chornack, Geologic Character of Tuffs in the Unsaturated Zone at Yucca Mountain, Southern Nevada, in *Role of the Unsaturated Zone in Radioactive and Hazardous Waste Disposal,* pp. 289-335, edited by J. Mercer, P. S. Rao, and I. W. Marine, Ann Arbor Science Publisher, Ann Arbor, MI, 1982.

Scotter, D. R. and P. Kanchanasut, Anion Movement in a Soil Under Pasture, *Aust. J. Soil Res.,* 19, pp. 299-307, 1981.

Sinnock, S., Y. T. Lin, and J. P. Brannen, Preliminary Bounds on the Expected, Postclosure Performance of the Yucca Mountain Repository Site, Southern Nevada, SAND84-1492, Sandia National Laboratories, Albuquerque, NM, 1984.

Spengler, R. W. and M. P. Chornack, Stratigraphic and Structural Characteristics of Volcanic Rocks in Core Hole USW-G4, Yucca Mountain, Nye County, Nevada, with a Section of Geophysical Logs by D. C. Muller and J. E. Kibler, USGS-OFR-84-789, U.S. Geological Survey, Denver, CO, 1984.

Thordarson, W., Geohydrologic Data and Test Results from Well J-13, Nevada Test Site, Nye County, Nevada, Water-Resources Investigations Report 83-4171, U.S. Geological Survey, Denver, CO, 1983.

Travis, B. J., S. W. Hodson, H. E. Nuttall, T. L. Cook, and R. S. Rundberg, Preliminary Estimates of Water Flow and Radionuclide Transport in Yucca Mountain, LA-UR-84-40, Los Alamos National Laboratory, Los Alamos, NM, 75 p, 1984.

van Genuchten, M. Th., A Closed-Form Equation for Predicting the Hydraulic Conductivity of Unsaturated Soils, *Soil Sci. Soc. Am. J.*, 44, pp. 892-898, 1980.

Wang, J. S. Y. and T. N. Narasimhan, Hydrologic Mechanisms Governing Fluid Flow in Partially Saturated, Fractured, Porous Tuff at Yucca Mountain, SAND84-7202, Sandia National Laboratories, Albuquerque, NM, LBL-18473, Lawrence Berkeley Laboratory, Berkeley, CA, *Water Resour. Res.*, 21, pp. 1861-1874, 1985.

Winograd, I. J. and W. Thordarson, Hydrogeologic and Hydrochemical Framework, South Central Great Basin, Nevada-California, with Special Reference to the Nevada Test Site, U.S. Geological Survey Professional Paper 712-C, pp. C1-126, 1975.

Appendix A

A Method for Approximating the Steady-State Hydraulic Head Profile in a One-Dimensional Vertical System

(Narasimhan, Alavi, and Tokunaga, 1985)

In steady-state, one-dimensional fluid flow, the volumetric flux density q is everywhere the same. For one-dimensional vertical flow, Darcy's Law can be written as

$$\vec{q} = -K(\psi,z)\frac{dh}{dz}\,\hat{z} \tag{1}$$

where $K(\psi, z)$ is the hydraulic conductivity (varying with both position z, as well as with matric/pressure head ψ) and $h = \psi + z$ is the hydraulic head.

Over a finite vertical distance Δz, the change in hydraulic head under steady-state conditions is

$$\Delta h = \Delta\psi + \Delta z = \frac{-q}{<K(\psi,z)>}\Delta z \tag{2}$$

where $<K(\psi,z)>$ is the averaged K over the interval Δz. Equation (2) is simply a rearrangement of Darcy's Law. Further rearrangement of Equation (2) gives

$$\Delta\psi_{ij} = -\left[1 + \frac{q}{<K>_{ij}}\right]\Delta z_{ij} \tag{3}$$

for the change in matric head in moving from $z = z_i$ to $z = z_j = z_i + \Delta z_{ij}$. By keeping the distance Δz_{ij} small enough so that $K(\psi,z)$ does not vary much within the interval, we have

$$\Delta\psi_{ij} \approx -\left[1+\frac{q}{K(\psi_i)}\right]\Delta z_{ij} \tag{4a}$$

$$\psi_j \approx \psi_i + \Delta\psi_{ij} \tag{4b}$$

$$h_j \approx h_i + \Delta\psi_{ij} + \Delta z_{ij} \quad . \tag{4c}$$

We apply the van Genuchten (1980) formula for $K(\psi)$ ($\psi \leq 0$)

$$K(\psi)_l = K_{sl} \frac{\left[1 - \frac{|\alpha_l \psi|^{n_l - 1}}{(1 + |\alpha_l \psi|^{n_l})^{m_l}}\right]^2}{\left[1 + |\alpha_l \psi|^{n_l}\right]^{0.5 m_l}} \tag{5a}$$

$$m_l = 1 - n_l^{-1}$$

$$l = \text{m (matrix)}, \; l = \text{f (fracture)}$$

in a weighted fashion for flow in fractured porous media as

$$K(\psi)_{bulk} = (1-\phi_l)\, K(\psi)_m + \phi_l\, K(\psi)_l. \tag{5b}$$

In Equations (5a) and (5b), K_s is the saturated hydraulic conductivity, α and n are constants for a given material, and ϕ_l is the fracture porosity in the composite medium.

Equations (4) and (5) are applied to the steady-state flow problems in the following way: q, $K(\psi,z)$, and one boundary potential are given. We wish to estimate the hydraulic head profile h(z) at steady state under the given conditions. We begin the approximation at the lower (water table) boundary, where $\psi = 0$. The datum for z is also chosen here at the water table. At this position, the steady-state q, K, and ψ are known exactly. Using this known $K = K_s(0)_{bulk}$, a Δz is selected so that K changes little over the interval. $\Delta\psi_{ij}$ is calculated from Equation (4a), and $\psi_j = \psi_i + \Delta\psi_{ij}$ is used in Equations (5a) and (5b) to estimate K_j (in this first Δz_{ij} interval $\psi_i = 0$). The K_j is compared with K_i (in this first step with $K_s(0)_{bulk}$). If $K_j \approx K_i$, the estimate of ψ_j is considered acceptable and h_j at $z = z_j$ is estimated with Equation (4c). When $K_j \not\approx K_i$, smaller Δz_{ij} were selected until $K_j \approx K_i$ was achieved. The K_j is then used in Equation (4a) to estimate $\Delta\psi_{jk}$ due to a further increment Δz_{jk}. This $\Delta\psi_{jk}$ is used to estimate ψ_k, from which K_k is obtained and to check for $K_k \approx K_j$. The procedure is repeated

for subsequent steps of Δz until the upper system boundary is reached. Estimates of h(z) are obtained at each Δz step. The h(z) are used as initial conditions in the program TRUST to minimize computation required to obtain the true steady-state head profile.

The acceptable range of K_j in the comparison $K_j \approx K_i$ was arbitrarily selected as about $0.3K_i < K_j < 3K_i$. Most K_j actually fell in the much tighter range of $0.7K_i < K_j < 1.3K_i$. Even more stringent control of the $K_j \approx K_i$ condition can be easily achievable.

Appendix B

Information Relevant to the Reference Information Base

B-1. Source of Data Used in the Report

1. Tables 1, 2 and 3 contain information for hydrologic data used in the report. All data were taken from Sinnock, Lin, and Brannen (1984), Peters et al. (1984), Ortiz et al. (1984), Nimick et al. (1984), Thordarson (1983), Spengler and Chornack (1984), and Wang and Narasimhan (1985). These reports were published before NNWSI Reference Information Base (RIB) instated.

2. Figure 1 through 6 are the plots based on the data in tables 1, 2 and 3.

3. Figure 9 is a conceptual grids of discrete fracture, porous matrix models.

B-2. Data Recommended for Inclusion Into the Reference Information Base.

No results are candidate for inclusion in the RIB.

B-3. Data Recommended for Inclusion Into the Tuff Data Base

None.

Distribution List

B. C. Rusche (RW-1)
Director
Office of Civilian Radioactive
Waste Management
U.S. Department of Energy
Forrestal Building
Washington, D.C. 20585

Ralph Stein (RW-23)
Office of Geologic Repositories
U.S. Department of Energy
Forrestal Building
Washington, D.C. 20585

J. J. Fiore (RW-22)
Program Management Division
Office of Geologic Repositories
U.S. Department of Energy
Forrestal Building
Washington, D.C. 20585

M. W. Frei (RW-23)
Engineering & Licensing Division
Office of Geologic Repositories
U.S. Department of Energy
Forrestal Building
Washington, D.C. 20585

E. S. Burton (RW-25)
Siting Division
Office of Geologic Repositories
U.S. Department of Energy
Forrestal Building
Washington, D.C. 20585

C. R. Cooley (RW-24)
Geosciences & Technology Division
Office of Geologic Repositories
U.S. Department of Energy
Forrestal Building
Washington, D.C. 20585

V. J. Cassella (RW-22)
Office of Geologic Repositories
U.S. Department of Energy
Forrestal Building
Washington, D.C. 20585

T. P. Longo (RW-25)
Program Management Division
Office of Geologic Repositories
U.S. Department of Energy
Forrestal Building
Washington, D.C. 20585

Cy Klingsberg (RW-24)
Geosciences and Technology Division
Office of Geologic Repositories
U.S. Department of Energy
Forrestal Building
Washington, D.C. 20585

B. G. Gale (RW-25)
Siting Division
Office of Geologic Repositories
U.S. Department of Energy
Forrestal Building
Washington, D.C. 20585

R. J. Blaney (RW-22)
Program Management Division
Office of Geologic Repositories
U. S. Department of Energy
Forrestal Building
Washington, D.C. 20585

R. W. Gale (RW-40)
Office of Policy, Integration, and
Outreach
U.S. Department of Energy
Forrestal Building
Washington, D.C. 20585

J. E. Shaheen (RW-44)
Outreach Programs
Office of Policy, Integration and
Outreach
U.S. Department of Energy
Forrestal Building
Washington, D.C. 20585

J. O. Neff, Manager
Salt Repository Project Office
U.S. Department of Energy
505 King Avenue
Columbus, OH 43201

D. C. Newton (RW-23)
Engineering & Licensing Division
Office of Geologic Repositories
U.S. Department of Energy
Forrestal Building
Washington, DC 20585

O. L. Olson, Manager
Basalt Waste Isolation Project Office
U.S. Department of Energy
Richland Operations Office
P. O. Box 550
Richland, WA 99352

D. L. Vieth, Director (4)
Waste Management Project Office
U. S. Department of Energy
Post Office Box 14100
Las Vegas, NV 89114

D. F. Miller, Director
Office of Public Affairs
U.S. Department of Energy
P. O. Box 14100
Las Vegas, NV 89114

P. M. Bodin (12)
Office of Public Affairs
U.S. Department of Energy
P. O. Box 14100
Las Vegas, NV 89114

B. W. Church, Director
Health Physics Division
U. S. Department of Energy
P. O. Box 14100
Las Vegas, NV 89114

Chief, Repository Projects Branch
Division of Waste Management
U.S. Nuclear Regulatory Commission
Washington, D.C. 20555

Document Control Center
Division of Waste Management
U.S. Nuclear Regulatory Commission
Washington, D.C. 20555

S. A. Mann, Manager
Crystalline Rock Project Office
U.S., Department of Energy
9800 South Cass Avenue
Argonne, IL 60439

K. Street, Jr.
Lawrence Livermore National
Laboratory
P. O. Box 808
Mail Stop L-209
Livermore, Ca 94550

L. D. Ramspott (3)
Technical Project Office for NNWSI
Lawrence Livermore National
Laboratory
P. O. Box 808
Mail Stop L-204
Livermore, Ca 94550

W. J. Purcell (RW-20)
Office of Geologic Repositories
U.S. Department of Energy
Forrestal Building
Washington, DC 20585

D. T. Oakley (4)
Technical Project Officer for NNWSI
Los Alamos National Laboratory
P.O. Box 1663
Mail Stop F-619
Los Alamos, NM 87545

W. W. Dudley, Jr. (3)
Technical Project Officer for NNWSI
U.S. Geological Survey
P.O. Office Box 25046
418 Federal Center
Denver, CO 80225

NTS Section Leader
Repository Project Branch
Division of Waste Management
U.S. Nuclear Regulatory Commission
Washington, D.C. 20555

V. M. Glanzman
U.S. Geological Survey
P.O. Box 25046
913 Federal Center
Denver, CO 80225

P. T. Prestholt
NRC Site Representative
1050 East Flamingo Road
Suite 319
Las Vegas, NV 89109

M. E. Spaeth
Technical Project Officer for NNWSI
Science Applications
International Corporation
Suite 407
101 Convention Center Drive
Las Vegas, NV 89109

SAIC-T&MSS Library (2)
Science Applications
International Corporation
Suite 407
101 Convention Center Drive
Las Vegas, NV 89109

W. S. Twenhofel, Consultant
Science Applications
International Corp.
820 Estes Street
Lakewood, CO 89215

A. E. Gurrola
General Manager
Energy Support Division
Holmes & Scisson, Inc.
P. O. Box 14340
Las Vegas, NV 89114

J. A. Cross, Manager
Las Vegas Branch
Fenix & Narver, Inc.
P.O. Box 15408
Las Vegas, NV 89114

Neal Duncan (RW-44)
Office of Policy, Integration,
and Outreach
U.S. Department of Energy
Forrestal Building
Washington, DC 20585

J. S. Wright
Technical Project Officer for NNWSI
Westinghouse Electric Corporation
Waste Technology Services Division
Nevada Operations
P.O. Box Box 708
Mail Stop 703
Mercury, NV 89023

ONWI Library
Battelle Columbus Laboratory
Office of Nuclear Waste Isolation
505 King Avenue
Columbus, OH 43201

W. M. Hewitt, Program Manager
Roy F. Weston, Inc.
2301 Research Blvd., 3rd Floor
Rockville, MD 20850

H. D. Cunningham
General Manager
Reynolds Electrical &
Engineering Co., Inc.
P.O. Box Box 14440
Mail Stop 555
Las Vegas, NV 89114

T. Hay, Executive Assistant
Office of the Governor
State of Nevada
Capitol Complex
Carson City, NV 89710

R. R. Loux, Jr., Director (3)
Nevada Agency for Nuclear Projects
Nuclear Waste Project Office
State of Nevada
Capitol Complex
Carson City, NV 89710

C. H. Johnson, Technical
Program Manager
Nevada Agency for Nuclear Projects
Nuclear Waste Project Office
State of Nevada
Capitol Complex
Carson City, NV 89710

John Fordham
Desert Research Institute
Water Resources Center
P.O. Box 60220
Reno, NV 89506

Department of Comprehensive
Planning
Clark County
225 Bridger Avenue, 7th floor
Las Vegas, NV 89155

Lincoln County Commission
Lincoln County
P.O. Box 90
Pioche, NV 89043

Community Planning and
Development
City of North Las Vegas
P.O. Box 4086
North Las Vegas, NV 89030

City Manager
City of Henderson
Henderson, NV 89015

N. A. Norman
Project Manager
Bechtel National Inc.
P.O. Box 3965
San Francisco, CA 94119

Flo Butler
Los Alamos Technical Associates
1650 Trinity Drive
Los Alamos, New Mexico 87544

Timothy G. Barbour
Science Applications
International Corporation
1626 Cole Blvd., Suite 270
Golden, CO 80401

E. F. Binnal
Field Systems Group Leader
Building 50B/4235
Lawrence Berkeley Laboratory
Berkeley, Ca 94720

Dr. Martin Mifflin
Desert Research Institute
Water Resouces Center
Suite 1
2505 Chandler Avenue
Las Vegas, NV 89120

Planning Department
Nye County
P.O. Box 153
Tonopah, NV 89049

Economic Development
Department
City of Las Vegas
400 East Stewart Avenue
Las Vegas, NV 89101

Director of Community
Planning
City of Boulder City
P.O. Box 367
Boulder City, NV 89005

Commission of the
European Communities
200 Rue de la Loi
B-1049 Brussels
BELGIUM

Technical Information Center
Roy F. Weston, Inc.
2301 Research Boulevard,
Third Floor
Rockville, MD 20850

R. Harig
Parsons Brinkerhoff Quade &
Douglas, Inc.
1625 Van Ness Avenue
San Francisco, Ca 94109-3678

Dr. Madan M. Singh, President
Engineers International, Inc.
98 East Naperville Road
Westmont, IL 60559-1595

6300 R. W. Lynch
6310 T. O. Hunter
6310 22/12141/64-5958/REP/TBD
6311 L. W. Scully
6311 C. Mora
6312 F. W. Bingham
6312 R. R. Peters
6313 T. E. Blejwas
6314 J. R. Tillerson
6315 S. Sinnock
6315 Y. T. Lin (5)
6332 WMT Library
6430 N.R. Ortiz
1511 R. R. Eaton
3141 S. A. Landenberger (5)
3151 W. L. Garner (3)
8024 P. W. Dean
3154-3 C. H. Dalin (28)
for DOE/OSTI